Frequency effects in the dynamic lateral stiffness of monopiles in sand: insight from field tests and 3D FE modelling

Kementzetzidis, E.; Metrikine, A.; Versteijlen, Willem Geert; Pisano, F.

DOI
10.1680/jgeot.19.ti.024

Publication date
2020

Document Version
Accepted author manuscript

Published in
Geotechnique: international journal of soil mechanics

Citation (APA)
Kementzetzidis, E., Metrikine, A., Versteijlen, W. G., & Pisano, F. (2020). Frequency effects in the dynamic lateral stiffness of monopiles in sand: insight from field tests and 3D FE modelling. *Geotechnique: international journal of soil mechanics*, *71*(9), 812-825. https://doi.org/10.1680/jgeot.19.ti.024

Géotechnique **00**, 1–15 [http://dx.doi.org/10.1680/geot.XX.XXXXX]

Frequency effects in the dynamic lateral stiffness of monopiles in sand: insight from field tests and 3D FE modelling

E. KEMENTZETZIDIS*, A.V. METRIKINE*, W.G. VERSTEIJLEN†, F. PISANÒ*

With the offshore wind industry rapidly expanding worldwide, geotechnical research is being devoted to foundation optimisation – most intensively for large-diameter monopiles. The analysis and design of monopiles still suffers from significant uncertainties in relation to cyclic/dynamic loading conditions. This work aims to shed new light on dynamic soil-monopile interaction, based on the results of unique full-scale experiments performed at the Westermeerwind wind park (Netherlands). The response of a 24 m long, 5 m diameter monopile to harmonic lateral loading of varying amplitude and frequency is inspected. The analysis of original field measurements (soil accelerations and pore pressures) enables to link the lateral stiffness observed at the monopile head to dynamic effects occurring in the surrounding soil. The interpretation of measured data is supported by three-dimensional finite element studies, also looking at the influence of drainage conditions and monopile size. The set of results presented supports the need for dynamics-based monopile design as higher frequencies gain relevance in most recent offshore wind developments.

KEYWORDS: piles & piling, sands, dynamics, full-scale tests, soil-structure interaction, finite-element modelling

INTRODUCTION

In recent years renewable energy resources have gained increasing relevance worldwide in the fight against climate change, in order to free human development from polluting fossil fuels. For example in the Netherlands, the Ministry of Economic Affairs has recently drawn a roadmap for CO2-neutral energy supply by 2050 (Dutch Ministry of Economic Affairs, 2016). The transition to renewables is regarded as one of the pillars for achieving CO_2-neutrality, a goal towards which public agencies, industry and academia, are currently collaborating.

The boom of the offshore wind market is continuing in Northern Europe and gradually expanding to other continents (Tsai *et al.*, 2016; Mattar & Borvarán, 2016; Archer *et al.*, 2017; Chancham *et al.*, 2017). Technological improvements have enabled the growth in size and capacity of offshore wind turbines (OWTs), along with remarkable cost reduction – notable examples of new-generation OWTs are General Electric's Haliade-X 12 MW and Siemens Gamesa's 14 MW turbines, featuring a rotor diameter of 220 m and 222 m, respectively. The trend towards installations in deeper waters and harsher environments poses significant technical challenges, especially regarding support structures and foundations (Pisanò & Gavin, 2017; Versteijlen, 2018). To date, about 80% of all OWTs installed in Europe are founded on monopiles, tubular steel piles of large diameter. Although alternative structural concepts are also receiving attention (e.g., jacket-supported or floating OWTs – Wang *et al.* (2018); Bienen *et al.* (2018); Arany & Bhattacharya (2018)), monopile-supported OWTs will continue to dominate the market in the foreseeable future as a low-risk solution (Kallehave *et al.*, 2015).

The uncertainties still associated with monopile design (Doherty & Gavin, 2012; Kallehave *et al.*, 2012) have given rise to valuable research projects, such as PISA in the UK (Byrne *et al.*, 2019), REDWIN in Norway (Skau *et al.*, 2018) and, in the Netherlands, DISSTINCT (Versteijlen *et al.*, 2017a). One of the main open questions in monopile design concerns the effects of installation on the operational performance. At present, most monopiles are driven into the soil by impact hammering, a method believed to highly influence the state of the soil around the monopile shaft and under the tip. Interesting steps towards quantifying installation effects have been recently taken (Tehrani *et al.*, 2016; Anusic *et al.*, 2017; Galavi *et al.*, 2017; Fan *et al.*, 2019), although with no wide consensus about long-term consequences. The above-mentioned DISSTINCT project used dynamic load tests on a full-scale, impact-driven monopile to address a number of interrelated questions (Versteijlen *et al.*, 2017b): are (pre-installation) soil properties from site investigation relevant to (post-installation) soil-monopile interaction? Are existing prediction models adequate to capture such interaction as it occurs in the field? Would field tests on a single monopile provide sufficient insight into real dynamic behaviour, and enable cost optimisation at the wind park scale?

In the past decades, a number of authors have studied the dynamic interaction between soil and (slender) piles, originally in relation to vibrating machines, bridge piers, and earthquakes (Novak, 1974; Kuhlemeyer, 1979; Kagawa & Kraft, 1980; Angelides & Roesset, 1981; Dobry & Gazetas, 1988; Gazetas & Dobry, 1984a; Mylonakis & Gazetas, 1999; Shadlou & Bhattacharya, 2014). More recently, contributions about short monopiles and caissons for OWTs have also appeared in the literature (Houlsby *et al.*, 2005, 2006; Shadlou & Bhattacharya, 2016; He *et al.*, 2019). DISSTINCT added to this research thread through a field investigation on monopile behaviour under loading frequencies larger than currently considered in offshore design. Indeed, the range of relevant loading frequencies is gradually expanding beyond 0.5 Hz, mostly due to OWTs being built in seismically active regions, and/or exposed to

---

Manuscript received...

* Faculty of Civil Engineering and Geosciences, Delft University of Technology, Stevinweg 1, 2628 CN Delft (The Netherlands)
† Siemens Gamesa Renewable Energy, Prinses Beatrixlaan 800, 2595 BN, Den Haag (The Netherlands)

'breaking & slamming' sea waves in deeper waters (Paulsen *et al.*, 2019). This paper reviews full scale field test results (DISSTINCT) with support from three-dimensional (3D) finite element (FE) modelling (Pisanò, 2019). Focus is on the frequency-dependence of the lateral monopile stiffness as observed in the field during low-amplitude vibrations. Field data and numerical simulation results are critically compared to explore the role of relevant dynamic effects, such as structural resonance(s) in the embedded monopile and pore pressure variations in the surrounding soil.

FULL-SCALE FIELD TESTS

The present work builds on the results of full-scale field tests performed in the framework of DISSTINCT (*Dynamic Interaction between Soil & Structures, Tools & Investigations using Numerical Calculation & Testing*), a 4-years collaborative project (2014-2018) involving TU Delft, Siemens Gamesa Renewable Energy, DNG-GL, Fugro, SWP and MBO Offshore. Methodology and main outcomes of the experimental programme are briefly outlined in this section, while more details can be found in Versteijlen *et al.* (2017b) and Versteijlen (2018).

Dynamic load tests were executed on a monopile at the Westermeerwind wind farm, located in the Netherlands on the eastern shore of the IJsselmeer lake (Figure 1). The monopile was 5 m in diameter and embedded under water in prevalently sandy soil for 24.05 m (L_{emb}) of its length ($L = 33.9$ m) – Figures 2–3.

Fig. 1. Location of the Westermeerwind wind farm (square).

Site characterisation

The wind farm site was characterised by combining seismic cone penetration tests (SCPTs) and boreholes. Within the shallowest 30 m (cf. to $L_{emb} = 24.05$ m), in situ tests confirmed the presence of medium-dense to dense sand ($D_R \approx 60 - 85\%$), with interleaved thin layers of peat and stiff clay at about 1 m and 20 m depth below the mudline, respectively – see Figure 2 regarding the SCPT45 test performed at the monopile location shown in Figure 1. Additional information about soil permeability at the site was inferred by the results of two HPT-CPTs (Hydraulic Profiling Tests) and one slug test executed near the monopile. The results of these tests returned a continuous permeability profile, featuring average sand permeability of approximately 1.4×10^{-4} m/s.

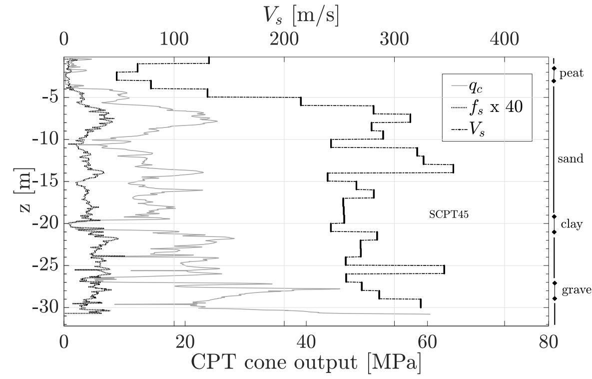

Fig. 2. Site characterisation near the monopile location based on SCPT tests and borehole data (right side, straight line denotes presence of sand) – q_c: cone resistance, f_s: sleeve friction, V_s: shear wave velocity. Modified after Versteijlen *et al.* (2017b).

At the IJsselmeer lake the Appelscha geological formation is known to create a rigid bedrock at depths ranging from 60 to 100 m. This information enables estimation of the multiple resonance frequencies associated with vertical shear wave propagation:

$$f_n = \frac{(2n-1)V_s}{4H} \tag{1}$$

where the n^{th} resonance frequency depends on the shear wave velocity V_s and the bedrock depth H. Inferring from Figure 2 a representative V_s of 300 m/s, the first resonance of the sandy deposit is expected to lie in the range between 0.75 and 1.25 Hz (Versteijlen *et al.*, 2017b).

Field testing procedures and measurements

After impact pile driving, dynamic lateral load tests were executed by placing a vibratory device at the top of the monopile as depicted in Figure 3 – a shaker consisting of two hydraulically powered large cogwheels. The shaker was able to deliver a maximum hydraulic power of 50 kW and rotate at a maximum frequency of 8.6 Hz. Steel plates were attached over the cogwheels at varying radial distance, and three different weight setups were considered to study the influence of the loading amplitude. Detailed studies delivered accurate estimates of effective lever arm (R) and rotating mass (m_e) associated with each set-up (Versteijlen, 2018). The total force $F(t)$ applied to the monopile head can thus be calculated as a function of the angular frequency of mass rotation (Ω, [rad/s]):

$$F(t) = m_e \Omega^2 R \sin(\Omega t) \tag{2}$$

where t denotes time. Different load cases were set up, and of particularly relevance to this paper were those involving a step-wise increase in excitation frequency. For each mass configuration, the duration of each frequency step was deemed sufficient to approach steady-state conditions. Three steel plates of different mass were used to generate the experimental scenarios summarised in Table 1. It was also evaluated that DISSTINCT shaking tests loaded the pile with forces much lower than those to be later transmitted by the installed OWT, and therefore well below the lateral capacity of the foundation.

Setup	$m_e \times R$ [mkg]	Frequency range [Hz]	Force range [kN]
Heavy weight	239.32	1.04 - 4.03	10.31 - 153.42
Middle weight	88.76	1.06 - 6.70	3.95 - 157.31
Light weight	32.08	5.04 - 8.68	32.15 - 95.40

Table 1. Technical specifications for the DISSTINCT load cases considered in this study.

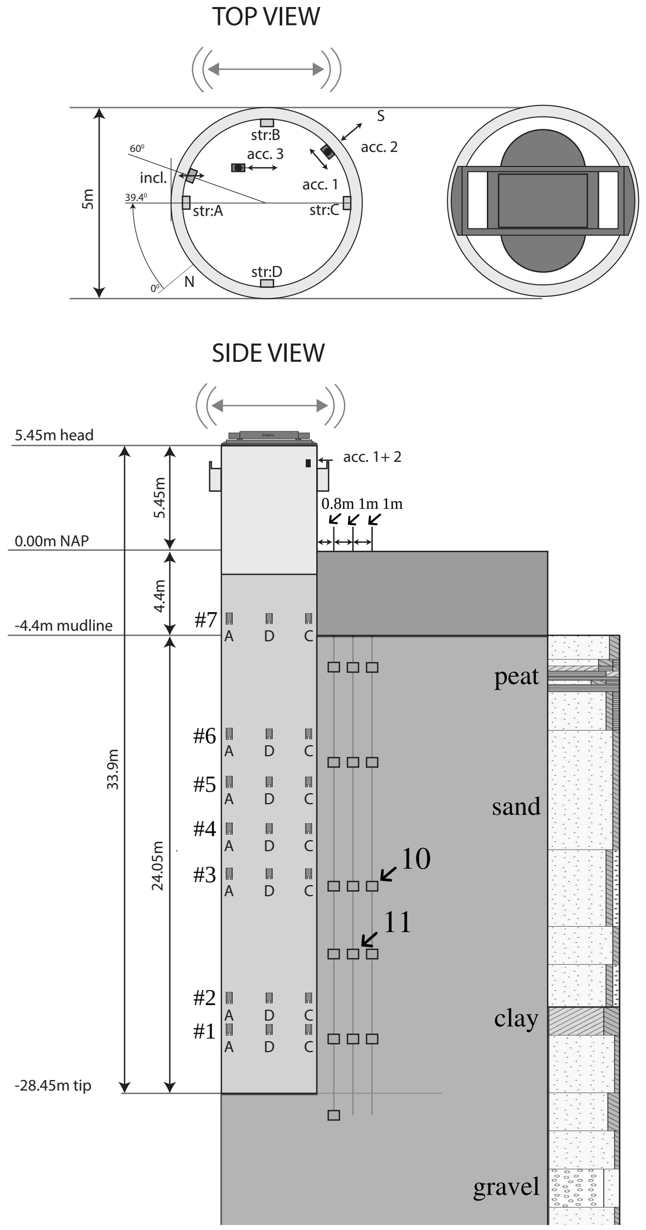

Fig. 3. Measurement setup. Depth values correspond with the NAP (Dutch equivalent of Mean Sea Level). Square markers in the soil region indicate locations of soil sensors, i.e. cones equipped with accelerometers and pore water transducers. Numbering along the pile (e.g. #1, #2, etc.) refers to arrays of strain gauges. Structural accelerations were measured both at the pile head and at the shaker. The locations of pore water and soil acceleration sensors 10 and 11 Arrows indicate the locations of pore pressure and acceleration sensors 10 and 11 in the soil – modified after Versteijlen *et al.* (2017b).

As illustrated in Figure 3, the response of the monopile was recorded through sensors installed on the pile and in the soil (Versteijlen *et al.*, 2017b; Versteijlen, 2018). Two Althen AAA320 accelerometers where placed on the pile head and one on the shaker, together with strain gauges along the monopile shaft. The soil response around the pile was detected by measuring local accelerations and variations in pore water pressure. The soil motion was recorded via 16 AS28/5g accelerometers capable of measuring accelerations lower than 1 gal. Variations in pore water pressure were recorded by means of fully analogue, 4-20 mA pressure transmitters of ATM/N type, endowed with a Wheatstone bridge circuit with analogue amplifier. It was thus possible to detect 'practically infinitesimal' pore pressure variations (very high resolution), and record maximum values up to 500 kPa with a deviation no larger than 0.3 kPa.

Experimental data

The analyses presented in this work are mainly based on acceleration data at the shaker and pore water pressure variations in the soil. Acceleration and pore pressure signals were post-processed by first removing their baseline (mean value), and then low-pass filtering at 10 Hz against high-frequency noise. All recorded data were interpreted by assuming the soil-monopile system to behave as a damped linear system at steady state for each frequency step. While the assumption of linearity was suggested by the weak loading amplitudes in Table 1, the attainment of stationary conditions in each frequency step was supported by good agreement with numerical simulation results based on the same assumption – see later. Overall, assuming steady-state linear response also justified the above-mentioned low-pass filtering of acceleration records. As free-vibration components would be eventually damped out, it seemed appropriate to focus on a relatively narrow frequency band around the main input spectrum (Table 1), so as to exclude most of the noise in sensor records. Filtered acceleration signals from the shaker and varying mass rotation frequency (henceforth, 'loading frequency') are illustrated in Figure 4 for the three test setups in Table 1.

As (linear) steady state theoretically implies vibrations at the same frequency Ω of the loading (Equation 2), it was possible to relate monoharmonic amplitudes of applied force $F(\Omega)$ and shaker displacement amplitudes ($\bar{U}$) from recorded data, with the latter obtained from acceleration amplitudes ($\ddot{\bar{U}}$) as:

$$\bar{U}(\Omega) = -\frac{\ddot{\bar{U}}(\Omega)}{\Omega^2} \tag{3}$$

Figure 5 illustrates (steady-state) relationships between applied forces and displacement amplitudes for the three loading scenarios (heavy, middle, light) – with frequency-dependence implicitly embedded into data points. The same data in Figure 5 are alternatively plotted in Figure 6a in terms of absolute value of the lateral dynamic stiffness ($|K_{dyn}|$) against the loading frequency. Data-based $|K_{dyn}|$ values were obtained as the ratio between the amplitudes of applied force and displacement at steady state.

The comparison between Figures 5 and 6a hints that, under the low loads considered (Table 1), the excitation

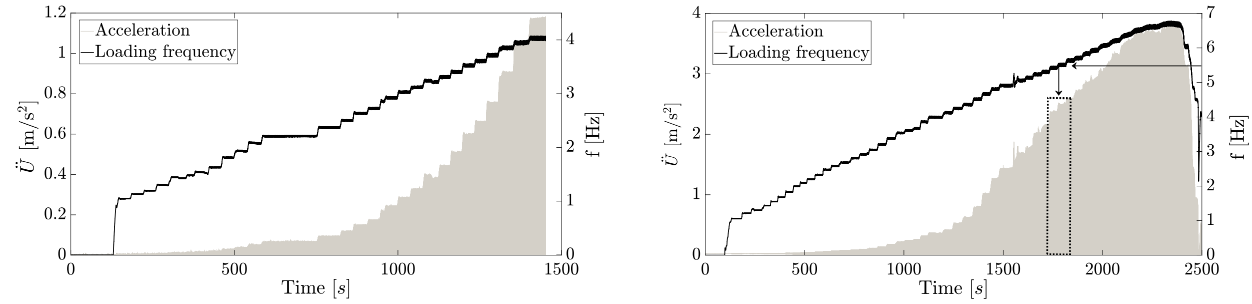

(a) Heavy weight

(b) Middle weight

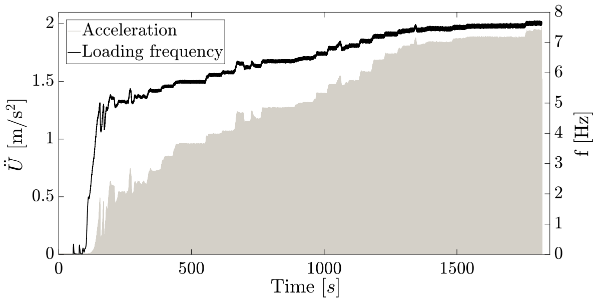

(c) Light weight

Fig. 4. Time evolution of accelerations ($\ddot{U}$) recorded at the shaker and loading frequency (f) for the three loading scenarios in Table 1. Only the positive side of acceleration diagrams are plotted for clarity. The dashed window in (b) highlights the response around 5.5 Hz.

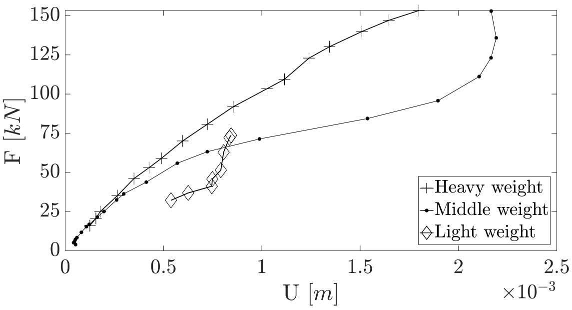

Fig. 5. Steady-state relationship between amplitude of the applied force (F) and displacement (U) at the shaker for the three loading scenarios in Table 1.

frequency impacts the pile lateral stiffness in a more profound manner than the loading amplitude. The dynamic pile head stiffness in Figure 6a appears clearly frequency-dependent, with a drop in $|K_{dyn}|$ of about 285% observed between 1-2 Hz and 5.3 Hz. As shown in Figure 6b, experimental data were then re-interpreted as if they resulted from a one degree-of-freedom (1dof) mass-damper-spring oscillator, featuring (static) stiffness, mass and damping coefficient equal to $K_0^{1dof} = 160$ MN/m, $M^{1dof} =$ 134 tons and $C^{1dof} = 1.482$ tons$\cdot s^{-1}$, respectively. Such settings in the equivalent 1dof system are associated with a resonance frequency of 5.5 Hz and a damping ratio $\zeta^{1dof} =$ 16%, whereas the absolute value of the 1dof dynamic stiffness $|K_{dyn}^{1dof}|$ was derived from the absolute value of the frequency response function $G(\Omega) = U(\Omega)/F(\Omega)$:

$$\begin{aligned} |K(\Omega)_{dyn}^{1dof}| &= 1/|G(\Omega)| = \\ &= \sqrt{(K_0^{1dof} - M^{1dof}\Omega^2)^2 + (C^{1dof}\Omega)^2} \end{aligned} \tag{4}$$

and then used to match the reduction in dynamic stiffness observed in experimental $|K_{dyn}|$ trends. The associated 1dof damping ratio of 16% may not be solely attributed to energy dissipation in the soil: generally, input energy will be dissipated through several physical mechanisms, including material damping (in the soil and in the monopile) as well as wave radiation. It should also be noted that 1dof fitting is fully adequate up to its resonance frequency, while $|K_{dyn}|$ is clearly over-predicted beyond that point. The physical nature of such resonance is discussed later on.

Interpretation of strain gauge data

Data from the strain gauges along the monopile supported the interpretation of the structural response during all shaking tests. For example, Figure 7 reports 2 seconds of axial strains associated with the middle weight setup towards the end of the 5.5 Hz frequency step – the frequency at which the lowest $|K_{dyn}|$ is observed. Same as for the acceleration signals, strain data were also low-pass filtered at 10 Hz and corrected for mean offset. The strain time histories in Figure 7 relate to sensors from 2A to 7A (Figure 3). The highest pile bending moment is expected to occur where the highest axial strain is recorded, i.e. at sensor 6A. Importantly, all strain gauges recorded at 5.5 Hz simultaneous compression and extension along the same side of the monopile, meaning that the stiffness degradation in the $|K_{dyn}|$ frequency-dependence is associated with the first bending mode.

Assessment of soil measurements

As previously mentioned, an array of accelerometers and pore-pressure sensors were installed in the soil near the monopile. As for pore pressure measurements, most attention was devoted to transient variations (Δp_w) with respect to pre-shaking, hydrostatic values. Generally, low

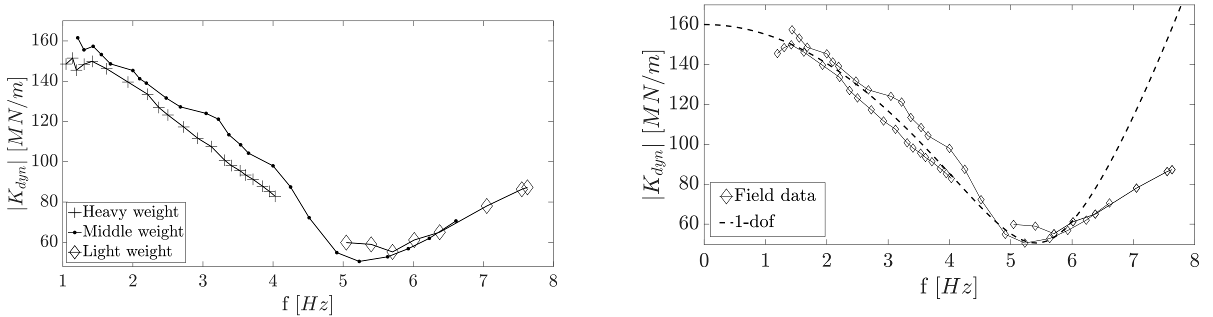

(a) from post-processing of field data for the three loading scenarios in Table 1.

(b) 1dof fitting of field data – static stiffness: K_0^{1dof} =160 MN/m, damping: $\zeta^{1dof} = 16\%$, resonance frequency: f_{res}=5.56 Hz.

Fig. 6. Frequency-dependence of the dynamic lateral stiffness $|K_{dyn}|$ observed at the monopile head.

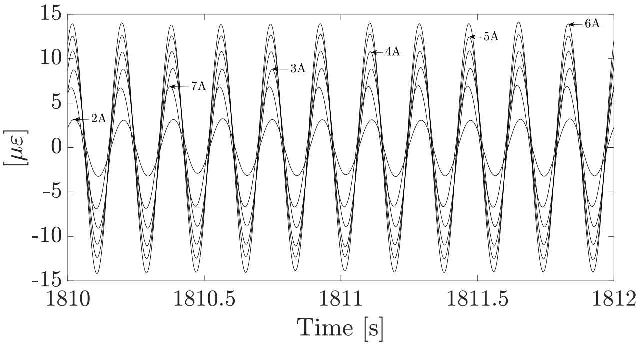

Fig. 7. Axial strains (ϵ) recorded along the monopile for the middle weight setup at the loading frequency of 5.5 Hz.

levels of soil acceleration ($\ddot{u}$) and pore pressure variations were recorded for the low-amplitude loads applied by the shaker, in the order of 0.1-0.2 m/s^2 and 0.5 kPa, respectively. Only pore pressure measurements in strong correlation with pile shaking were considered after selection based on the following procedure:

1. both soil acceleration and pore pressure signals were low-pass filtered at 10 Hz (see Figures 8a-8b), then normalised with respect to their maxima;
2. cross-correlation functions were numerically determined for pairs of (normalised) acceleration and pore pressure signals, so as to objectively quantify signal similarity;
3. only pore pressure measurements highly correlated with soil motion were deemed reliable.

The above procedure led to 'approve' only those sensors ensuring high cross-correlation between pore pressure variation and acceleration. For the middle weight setup taken as main reference, this prerequisite was only fulfilled by sensors 10 and 11 in Figure 3. For both sensors, correlations between pore pressure variations and horizontal accelerations were very similar regardless of the direction (x or y) – the cross-correlations shown in Figure 8 relate to measured accelerations projected along the loading direction.

3D FE MODELLING

3D FE analysis is proving increasingly valuable to modern offshore wind developments, in that it can support the understanding of complex geotechnical mechanisms, as well as the conception of engineering design methods (Kementzetzidis *et al.*, 2018, 2019; Pisanò, 2019; Byrne *et al.*, 2019). 3D FE modelling was carried out through the OpenSees simulation platform (McKenna, 1997), however with no need for advanced, non-linear modelling of soil behaviour. As DISSTINCT field tests were performed by applying low-amplitude vibrations, the soil was idealised as a water-saturated, linear elastic, porous medium, with hydro-mechanical coupling effects possibly taking place depending on well-known governing factors (Zienkiewicz *et al.*, 1999).

Numerical studies were conducted at two levels, aiming to investigate the response of soil-monopile system as a whole, but also the dynamics of the site prior to pile installation ('soil-only' analyses). The following three types of FE dynamic analyses were performed:

- soil deposit subjected to harmonic horizontal loading at the free surface;
- soil deposit subjected to harmonic vertical loading at the free surface;
- soil-monopile system subjected to harmonic horizontal loading at the monopile head as during the reference shaking tests.

In all cases sinusoidal point loads were applied until the attainment of steady state (total duration up to 120 seconds in some cases), with loading frequency ranging from 0 to 7.5 Hz and load application point shown in Figure 10.

Governing equations and space/time discretisation

The 3D FE model was built on the Biot-Zienkiewicz *u-p* coupled formulation described in Zienkiewicz *et al.* (1980), particularly in the simplified 'consolidation form' studied by Chan (1988). Such formulation enabled analysis of the extreme hydromechanical bounds of fully drained and undrained response with a single model, by setting either very high or very low soil permeability in the coupled FE model. As shown in the Appendix, a *u-p* model of the form referred to, produces results that are equivalent to the outcome of a one-phase/drained model as the permeability tends to infinity (i.e., to very high values). Given the assumption of linear elastic behaviour, the properties of the soil skeleton were directly inferred from site investigation data (SCPT45, Figure 2) to characterise the stratigraphy shown in Figure 9. The typical value of $K_f = 2.2 \cdot 10^6$ kPa was assigned to the bulk modulus of the pore water. The

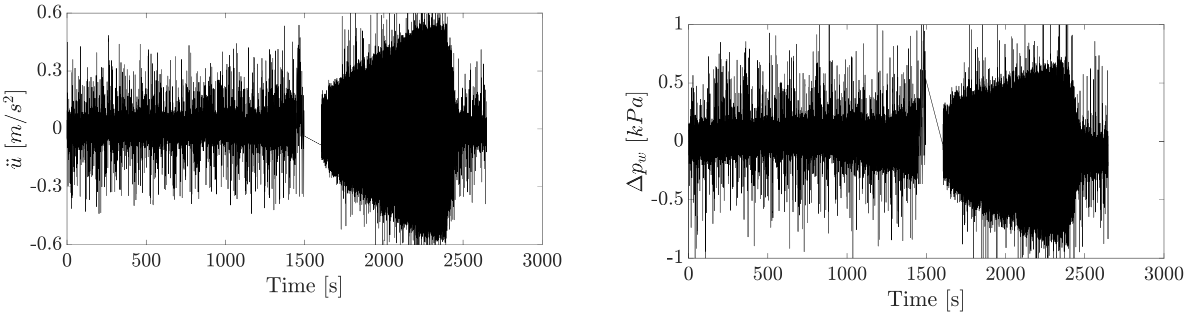

(a) filtered acceleration ($\ddot{u}$) (baseline removed) at sensor 10.

(b) filtered pore pressure variation Δp_w at sensor 10.

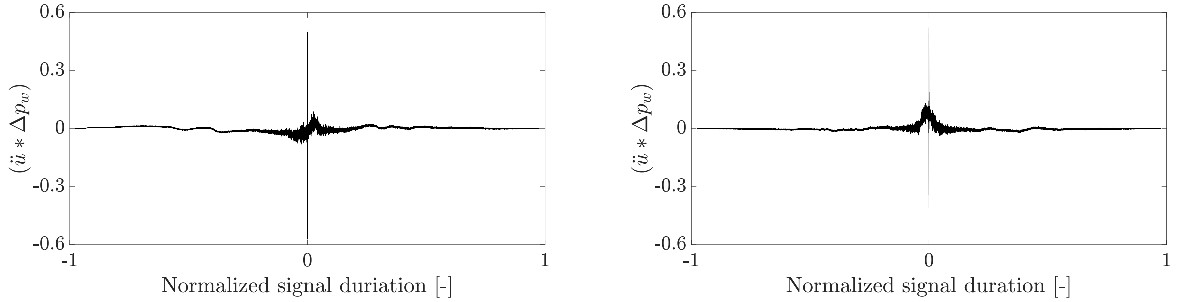

(c) acceleration-pressure cross-correlation for sensor 10.

(d) acceleration-pressure cross-correlation for sensor 11.

Fig. 8. Comparative assessment of soil acceleration and pore pressure variation data for the middle weight load setup in Table 1. Data gaps in (a) and (b) around 1500 s were caused by partial corruption of original data files. (c) & (d) show the cross-correlation between acceleration-pore water pressure signals ($\ddot{u} * \Delta p_w$) for sensors 10 and 11.

geometrical/loading symmetry of the problem was exploited to build a less expensive half-model.

The soil domain was discretised using the eight-node H1-P1ssp stabilised elements developed by McGann *et al.* (2015), featuring equal-order, linear interpolation of both displacement and pore pressure unknowns. The benefits of H1-P1ssp elements in relation to soil-monopile simulations are described by Corciulo *et al.* (2017), and include the stabilisation of pore pressure instabilities as undrained conditions are approached. Space discretisation was set to ensure appropriate propagation of harmonics up to 8 Hz, so that no less than 7–8 elements per wavelength were guaranteed in that frequency range. The standard Newmark integration algorithm was selected for time stepping, with integration parameters β and γ equal to 0.6 and 0.3025, respectively (Hughes, 1987). A time-step size of $\Delta t = 8.3 \times 10^{-4} s$ was found appropriate after numerical sensitivity studies (Watanabe *et al.*, 2017) – not reported for brevity.

To alleviate computational costs, it was not attempted to model the real location of the bedrock at the IJsselmeer lake, about 100 m below the mudline. This choice was noted to affect the simulated dynamics of the soil deposit (and in turn of soil-monopile interaction), however with no serious impact on the general conclusions drawn later on in this study.

Structural modelling of shaker and monopile

The embedded portion of the monopile was modelled as a 3D steel continuum and discretised by means of one-phase, eight-node ssp bricks (McGann *et al.*, 2015). Conversely, the above-mudline part was modelled as an elastic beam and discretised through twenty Timoshenko beam elements ($\approx$ 50 cm each), featuring consistent (non-diagonal) mass matrix. The mass of the shaker M_{sh} was lumped at the top of the monopile – see Figure 10. Added mass effects associated with surrounding sea water were simplistically introduced in the form of nodal lumped masses evenly distributed along the water depth $H_w \approx 4.5$m (Figure 3), and calculated as twice the water mass in the submerged OWT volume (Newman, 1977).

The soil model use here was relatively simplistic in that it was not designed to capture installation effects or the non-linear frictional behaviour of the soil-pile interface. Although it is clearly unrealistic to assume perfect soil-pile bonding, this choice allowed to preserve the intended linearity of the analyses, and avoided the assumption of input parameters which are not based upon specific soil characterisation. It was noticed, however, that interface properties may quantitatively affect dynamic soil-monopile interaction, especially at higher frequencies – this matter will receive further attention in future studies.

Energy dissipation in the numerical model

Energy dissipation (damping) plays an essential role in dynamic soil-structure interaction. OWTs dissipate energy during operations in multiple ways, such as:

- aerodynamic damping due to interaction between wind and rotating blades;
- hydrodynamic damping associated with monopile-water interaction;
- damping in structural materials (steel) and connections;
- damping in the soil arising from material dissipation, hydro-mechanical effects and wave radiation – see also Kementzetzidis *et al.* (2019).

In all FE simulations, aerodynamic and hydrodynamic damping were neglected, since no actual OWT tower was

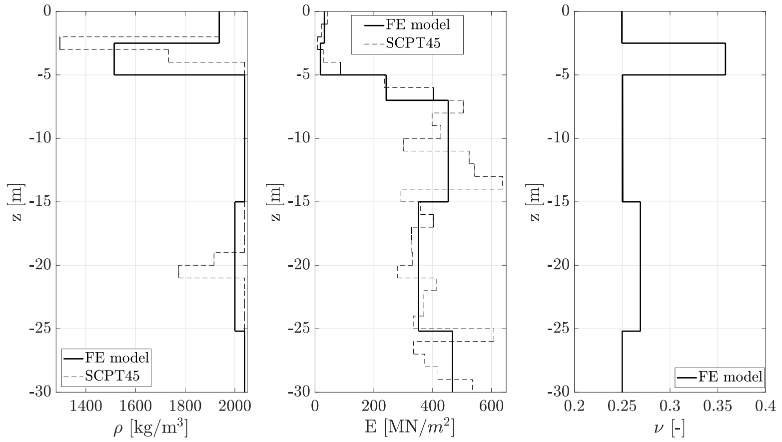

Fig. 9. Depth (z) profiles of saturated mass density (ρ) and elastic properties, Young's modulus (E) and Poisson's ratio ν, adopted in FE simulations.

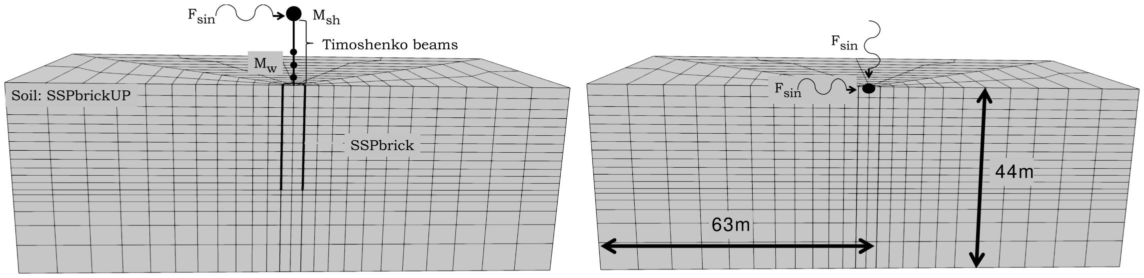

(a) shaker-monopile-soil **(b) soil-only**

Fig. 10. Discretised soil domain and loading settings in complete and 'soil-only' FE analyses.

present during the field tests in very shallow water depth (only 4.4 m above the mudline). It is also worth mentioning that:

- wave radiation through lateral domain boundaries was enabled based on the well-established approach by Lysmer & Kuhlemeyer (1969);
- with the soil modelled as a linear elastic material, no damping in the solid skeleton was accounted for, in reasonable agreement with the small amplitude vibrations associated with the load cases in Table 1. The use of Rayleigh damping to model dissipation in the soil skeleton at very small strains was not pursued, due to the lack of relevant data for calibration;
- (compressional) wave motion in saturated porous media is generally dissipative due to hydro-mechanical coupling effects – for instance, under the fully undrained conditions considered later on (Biot, 1956; Han *et al.*, 2016);
- steel damping in the monopile was introduced according to Eurocode 1 BS EN (1991), with (Rayleigh) damping ratio $\zeta_{steel} = 0.19\%$ at the pivotal frequencies of 0.1 and 80 Hz;
- numerical damping spontaneously arises from Newmark's time integration algorithm set up as mentioned above. Nonetheless, algorithmic dissipation proved beneficial in attenuating high-frequency spurious oscillations in the simulated response (Kontoe *et al.*, 2008).

FE-BASED INTERPRETATION OF FIELD DATA

This section elaborates on the interpretation of field observations based on 3D FE results.

'Soil-only' simulations

Preliminary 'soil-only' simulations were performed to investigate the dynamics of the reduced soil model, and quantify its influence on the response of the shaker-monopile-soil system. The layered soil domain was subjected to mono-harmonic loading, either horizontal or vertical (Figure 10), spanning the frequency range of interest from 0 Hz (static loading) to 8 Hz. Hydro-mechanical coupling effects were inhibited by setting an unrealistically high soil permeability of 10^6 m/s, i.e., sufficiently large to make the water-saturated soil behave as a one-phase porous medium of identical total mass density – see Appendix. Horizontal/vertical soil responses at steady state are illustrated in Figure 11 in terms of amplification factors $A = |\bar{u}_{dyn}|/u_{static}$ at the shaker location, and phase differences between applied load and predicted soil displacement – u_{static} represents the displacement computed under a static load of magnitude equal to the amplitude of the dynamic load.

Phase difference trends in Figure 11b show in-phase force-displacement oscillations until about 2.5 Hz and 4.5 Hz for horizontal and vertical loading, respectively. As is well-known, nil phase difference is indicative of a quasi-static response with no waves propagating in the domain. The frequencies numerically identified (2.5 Hz and 4.5 Hz) are usually referred to as 'cut-off' frequencies, and mark the transition from 'evanescent waves' (vibrations exponentially

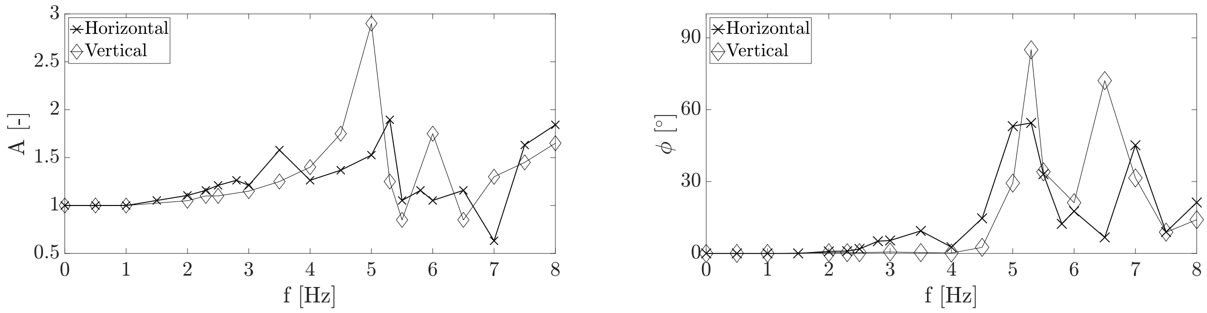

(a) Amplification factor (A) **(b) Phase difference (ϕ)**

Fig. 11. Simulated steady-state responses of the soil deposit to horizontal and vertical point loading at varying loading frequency (f).

decaying along the distance from the source) to actual wave motion (Graff, 2012). Overcoming the cut-off frequency also determines the onset of radiation damping, primary source of energy dissipation in the FE soil models set up in this work. Previous studies on radiation damping in 3D continua pointed out its dependence on excitation frequency, geometrical settings and mechanical properties (Berger *et al.*, 1977; Novak *et al.*, 1978; O'Rourke & Dobry, 1982; Gazetas & Dobry, 1984a,b; Shadlou & Bhattacharya, 2014). As mentioned above, the FE model is not fully representative of the real site configuration, where the rigid bedrock is significantly deeper than in the model. The shallower bedrock set for faster FE computations implies cut-off frequencies higher than expected at the real site, and therefore later onset of radiation damping and some over-prediction of dynamic amplification levels.

Dynamics of the shaker-monopile-soil system

Numerical eigenfrequency analysis

As a first step into understanding the response of the whole shaker-soil-monopile system, numerical eigenvalue analysis was carried out for the FE model in Figure 10. Due to the many degrees of freedom in the discretised system, the analysis returned multiple closely-spaced eigenfrequencies, including the first eigenvalue at 1.59 Hz associated with 'soil-only resonance'. Among the numerous numerical modes found in proximity of relevant frequencies (e.g., near the resonance frequency observed in field test results – ≈ 5.5 Hz), it was not straightforward to identify real physical modes. A heuristic mode-sorting procedure was set up by selecting eigenvectors showing significant lateral displacement of the monopile at the shaker location. Accordingly, three modes near the resonance peak were isolated at 5.67, 5.71 and 5.87 Hz – see graphical representation in Figure 12. In elastodynamics, each i^{th} mode contributes to the global response depending on the distance between external loading frequency Ω and related eigenfrequency ω_i, with a participation factor Γ_i that takes the following form for undamped multi-dof systems:

$$\Gamma_i = \frac{1}{\omega_i^2 - \Omega^2} \tag{5}$$

The above expression clarifies how the effect of the i^{th} mode on the global response vanishes for ω_i far from Ω.

Drained dynamic response

As for 'soil-only' simulations, the dynamic performance of the whole system was first analysed under fully drained conditions. Also in this case, pore pressure effects were prevented by setting high soil permeability ($k = 10^6$ m/s). There was no attempt to re-tune the soil properties in Figure 9 to improve the numerical simulation of field measurements.

Time domain analyses were performed for different loading frequencies within the selected range (0-7.5 Hz), then steady-state displacement amplitudes at the shaker and load-displacement phase differences were extracted. Drained FE results are compared to experimental data in Figure 13, and seem to capture well the overall frequency-dependence of the monopile stiffness. The minimum stiffness near 5.5 Hz is clearly reproduced, while simulations for frequencies lower than 2 Hz returned a gradual increase in dynamic stiffness as nearly static conditions are approached. On average, 3D FE results seem to slightly over-predict experimental stiffness values, most probably as a consequence of simplifying modelling assumptions.

Some sharp 'outliers' appear in the numerical results in the form of local stiffness drops at 2.5, 3.5 and even 5.5. Hz. Such outliers, not visible in experimental data, may be directly related to soil-only amplification (see Gazetas (1983)), as suggested by Figure 11a. In this respect, accurate modelling of the bottom rigid boundary would be key to improving numerical simulation results. Improved modelling of soil damping would also contribute to the same goal, in that it would smoothen the sharp outliers in Figure 13 (Gazetas, 1983). Although DISSTINCT data do not seem affected by pure soil resonance, it is worth noting that soil amplification in soft soils would likely be happening at frequencies lower than 0.5 Hz for bedrocks deeper than 100 m – i.e., within the frequency band considered in current design practice.

Further insight into FE results can be obtained by inspecting the phase difference between applied load and steady-state displacement at the shaker head. Figure 15 reveals significant increase in phase difference in the vicinity of 5.5. Hz. This observation suggests an analogy with the response of the equivalent 1dof oscillator depicted in Figure 6b, exhibiting a 90° phase shift at resonance. The agreement between FE and 1dof phase difference trends in Figure 15 clarifies the physical nature of the remarkable stiffness reduction at 5.5 Hz, which can be now attributed to global resonance in the shaker-monopile-soil system. Besides, the smoothness of experimental stiffness curves suggests that

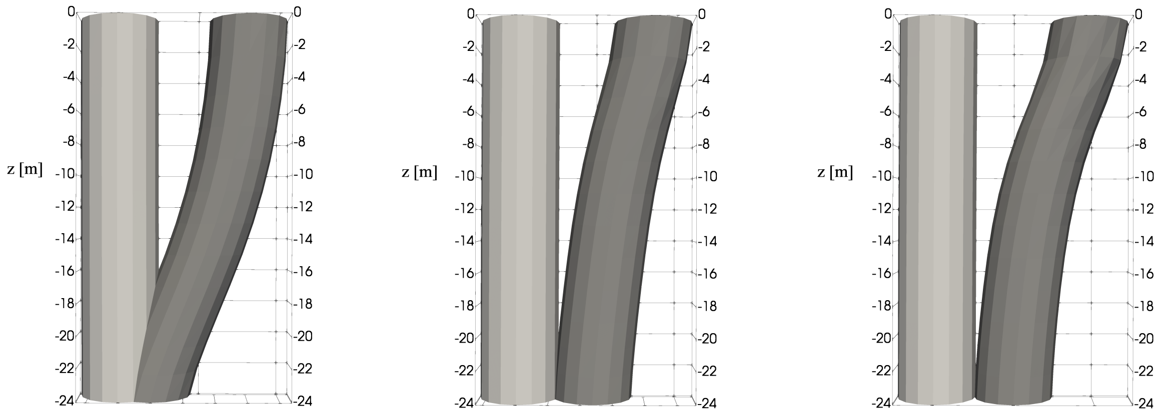

(a) 5.67 Hz **(b) 5.71 Hz** **(c) 5.87 Hz**

Fig. 12. Monopile (embedded) modal shapes for eigenvectors of the shaker-pile-soil system associated with eigenfrequencies close to experimental resonance ($\approx$ 5.5 Hz).

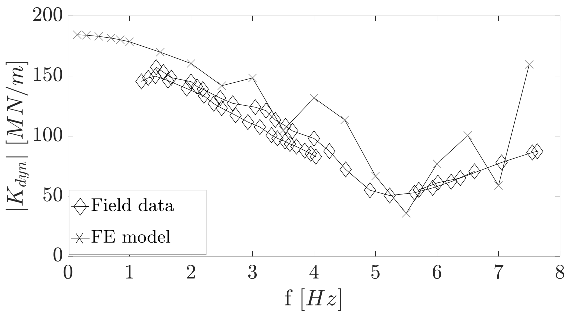

Fig. 13. Frequency dependence of monopile dynamic stiffness $|K_{dyn}|$ as emerging from field tests and FE modelling.

more energy dissipation occurred in the field tests than was reproduced by the FE model.

Also obtained from FE results is the steady-state deformed shape of the monopile at 5.5 Hz, resembling in Figure 14 the typical shape of a cantilever loaded at the free end. This outcome is in full agreement with the strain measurements in Figure 7. As none of the modes in Figure 12 represents accurately the dynamic deformed shape, the influence of several participating modes is deduced.

Undrained dynamic response

The FE results presented so far were obtained for fully drained conditions, i.e., by disregarding hydro-mechanical coupling effects in the soil. To assess the impact of such assumptions, the response of the system in the opposite undrained limit was numerically explored by assigning a vanishing permeability ($k = 10^{-18}$ m/s) to the whole soil domain. Accordingly, it was possible to simulate pore pressure variations caused by hindered water drainage.

As in the drained case, 'soil-only' simulations were first performed to clarify how the undrained dynamics of the soil deposit can impact the response to lateral harmonic loading of the shaker-monopile-soil system. The same approach described above for drained conditions was followed, i.e., horizontal and vertical monoharmonic point loads were applied until steady-state over a frequency range from 0 to 8 Hz. Undrained trends of amplification factor and phase difference for both loading directions are reported in Figures 16a–16b.

The undrained monopile-soil model was validated by comparing in Figure 17 the steady-state amplitudes of pore pressure variations simulated for different loading frequencies to the measurements from sensors 10-11 (Figure

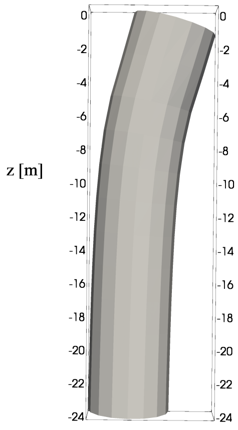

Fig. 14. Steady-state deformed shape of the monopile arising from 5.5 Hz FE calculations.

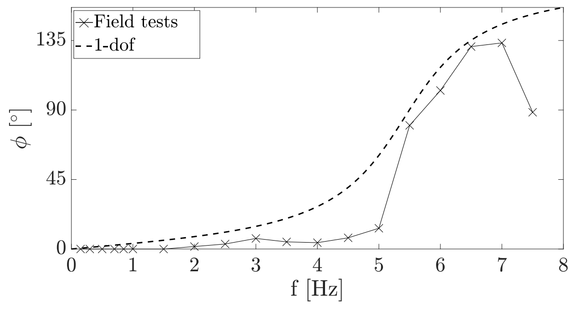

Fig. 15. Phase difference (ϕ) between applied load and steady-state shaker displacement from FE and equivalent 1dof results.

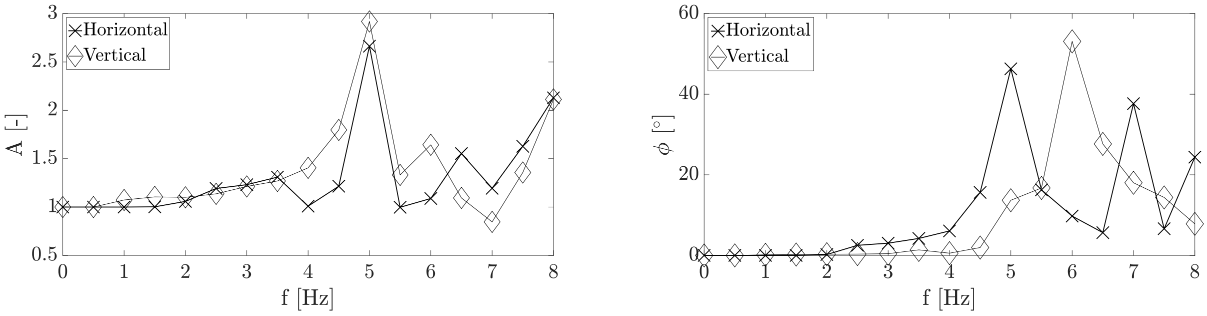

(a) Amplification factor (A) **(b) Phase difference (ϕ)**

Fig. 16. Simulated undrained steady-state responses of the soil deposit to horizontal and vertical point loading at varying loading frequency (f).

3) associated with the middle weight load case. As for the drained simulations, distinct mono-harmonic analyses were performed numerically until the attainment of steady-state; then, steady amplitudes of pore pressure variation were extracted (Figure 17c) for comparison to measured data – it was assumed that also pore pressure variations reached a steady state in each frequency step during field tests. Numerical steady-state amplitudes (e.g., from Figure 17c) were finally inserted in Figures 17a–17b over time intervals corresponding with relevant frequency steps. Computed and measured pore pressure variations share similar trends and reasonably similar values, confirming the suitability of the 3D FE model in its undrained version.

Figure 17 suggests that pore pressure effects can be very weak under low operational loads, and yet the common assumption of fully drained response in sand is not necessarily valid. The poro-elastic FE model enabled evaluation of the impact of hydro-mechanical coupling on the undrained dynamic stiffness of the monopile during small amplitude vibrations. Undrained model predictions are presented in Figure 18 together with previous drained results and experimental data. Generally, undrained conditions do not seem to significantly affect the dynamic stiffness trend, especially until the 5.5 Hz resonance. Particularly, sharp 'outliers' characterise also the undrained response trend, for instance at 4 and 7 Hz, in a way that can be again attributed to the undrained 'soil-only' amplifications visible in Figure 16a. Larger discrepancies among experimental, drained and undrained results arise in the post-resonance branch: such evidence hints that partial water drainage and relative soil-water accelerations may play a role in the monopile-soil interaction at sufficiently high frequencies. The investigation of such effects will require further refinement/generalisation of the u-p-based FE model adopted in this study.

Influence of monopile diameter

Monopile diameter is normally tuned by designers to achieve desired dynamic performance in terms of OWT first natural frequency. Additional FE calculations were performed for a larger monopile of 6 m diameter, so as to shift the natural frequency of the global system beyond the 'soil-only' resonances previously discussed.

Frequency-dependent values of amplification factor, phase difference, and dynamic lateral stiffness are plotted in Figure 19 for both diameters, 5 and 6 m. It is further confirmed that the amplification frequencies identified at 2.5 and 3.5 Hz are indeed of the 'soil-only' type (Figure 11a), therefore not affected by mononopile diameter. Additionally, the highest amplification peak for the 6 m diameter monopile occurs at a frequency lower than 5 Hz, and should be compared to the 5.5 Hz resonance hit by the 5 m monopile. This seemingly counter-intuitive outcome (a stiffer monopile may be expected to resonate at a higher frequency) can be explained via the phase difference curves in Figure 19b. Dynamic resonance is normally accompanied by input-output phase difference of 90° degrees, a circumstance that occurs at ≈5.6 Hz for the 5 m monopile, and near 6.8 Hz in the 6 m case – with an amplification peak lower than in the 5 m case. In light of this observation, it is recognised that the 6 m pile undergoes structural resonance near 6.8 Hz, though with an amplification lower than at 5 Hz. Such difference can only be caused by 'soil-only' amplification effects at 5 Hz, whose quantitative influence highlights the importance of accurate domain modelling in dynamic soil-structure interaction problems.

CONCLUDING REMARKS

The results of full-scale, dynamic field tests on a stiff monopile were examined to investigate the frequency-dependence of soil-pile interaction at a sandy site. To support the interpretation of field data, 3D FE modelling was undertaken, with soil parameters derived from pre-installation site data.

For the weak vibrations induced by the pile-shaking device, the good agreement between experimental and numerical results supported the soundness of most simplifying assumptions, such as the idealisation of linear elastic soil skeleton. Low variations in pore pressures (with respect to hydrostatic values) were predicted when modelling fully undrained conditions – another outcome compatible with field measurements. The latter observation confirmed the suitability of neglecting pore pressure effects for weakly loaded monopiles in sand; however, claiming that water drainage (and volume changes) are fully allowed in the soil around the pile may prove inaccurate in some cases. Obviously, the discussion about pore pressure effects will assume more relevance for higher load levels, under which soil non-linearity and cyclic effects are more pronounced (Kementzetzidis *et al.*, 2019; Liu *et al.*, 2019).

The dynamic response of the monopile exhibited remarkable frequency-dependency at loading rates higher than currently considered in design. Significant energy dissipation was also observed, with a global viscous damping ratio of about 16% deduced from field data. Wave radiation

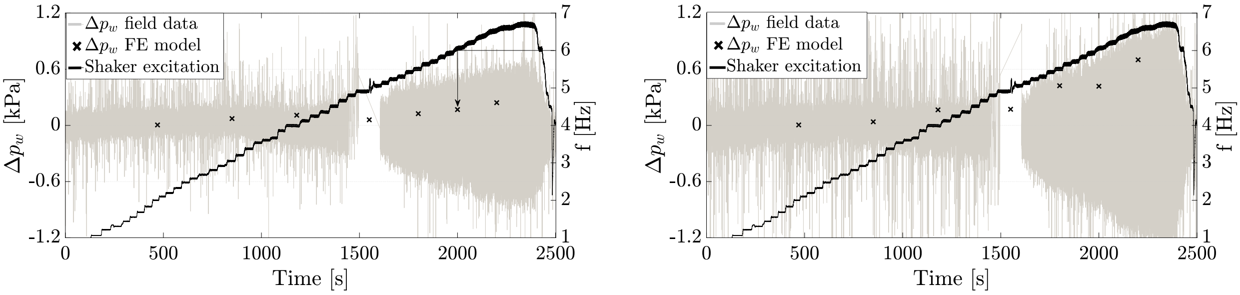

(a) measured pore pressure variations – sensor 10. **(b) measured pore pressure variations – sensor 11.**

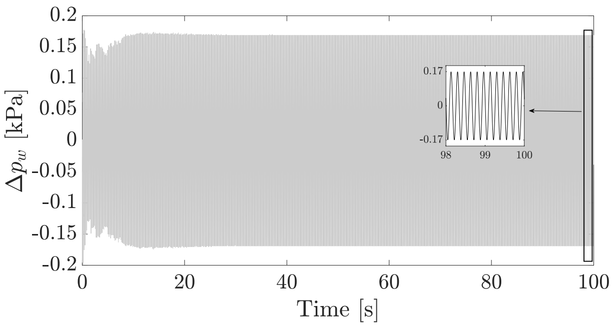

(c) simulation of pore pressure variation under 6 Hz harmonic loading at the location of sensor 10.

Fig. 17. Comparison between measured and simulated pore pressure variations (middle weight load case). The arrow in (a) points to a specific steady-state amplitude ($\Delta p_w = 0.17$ kPa), resulting from the numerical results illustrated in (c).

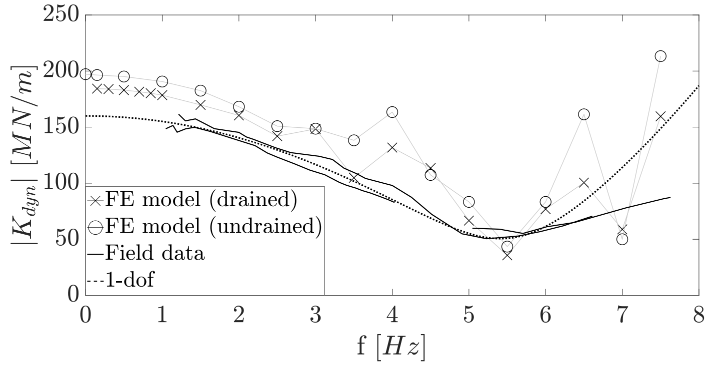

Fig. 18. Influence of drainage conditions on the monopile dynamic stiffness.

in the soil is believed to largely, but not exclusively, contribute to such dissipation.

Inspection of FE results under varying frequency, pile diameter and drainage conditions led to recognition of the wide range of soil-monopile interaction scenarios caused by dynamic effects. As larger turbines are installed in more dynamically-active environments (deeper waters and/or seismic regions), considerations regarding wave motion in the surrounding soil will become increasingly relevant to geotechnical design.

ACKNOWLEDGEMENTS

The authors express their gratitude to the DISSTINCT consortium (project number TKIW02001) for allowing full access to field data.

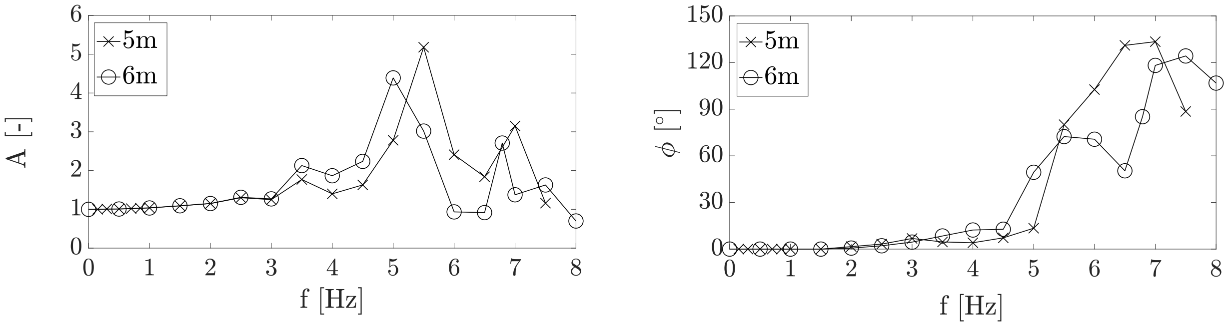

(a) Amplification factor (A)

(b) Phase difference (ϕ)

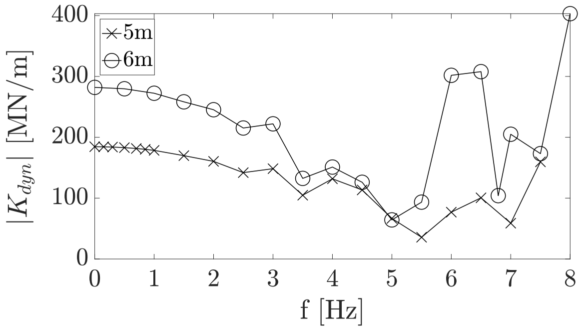

(c) Dynamic stiffness ($|K_{dyn}|$)

Fig. 19. Simulated steady-state responses of laterally loaded monopiles of 5 m and 6 m diameter.

LIST OF SYMBOLS

Greek symbols

β, γ	Newmark's time integration parameters
Γ_i	modal participation factor associated with i^{th} mode
Δp_w	pore water pressure variation
ε	axial strain
ζ^{1dof}	damping ratio of the equivalent 1dof system
ζ_{steel}	steel damping ratio
ν	soil Poisson's ratio
ρ	saturated mass density for sand
ρ_f	mass density of pore fluid
ρ_s	mass density of soil grains
$\sigma,\ \sigma'$	soil stress tensor (total and effective)
ϕ	phase difference/angle
Ω	angular excitation/loading frequency
ω_i	eigenfrequency associated with i^{th} mode

Latin symbols

A	amplification factor
C^{1dof}	viscous damping coefficient for the equivalent 1dof system
D	Soil stiffness tensor (D_{ijkl})
D_R	soil relative density
E	Young's modulus of elasticity
$\bar{E}$	1D (oedometer) stiffness modulus
F	applied load amplitude
f_s	CPT sleeve friction
f_n	n^{th} natural frequency of the soil deposit
f_{res}	resonance frequency
G	transfer function
g	Earth's gravity acceleration
H_w	water depth
K_{dyn}	lateral dynamic stiffness of the monopile
$\lvert K_{dyn}^{1dof} \rvert$	absolute value of the dynamic stiffness of the equivalent 1dof system
K_0^{1dof}	static stiffness of the equivalent 1dof system
K_f	fluid bulk modulus
K_s	soil grains bulk modulus
$k,\ k'$	soil permeability coefficients in the static and dynamic versions of Darcy law
L	monopile length
L_{emb}	embedded monopile length
M^{1dof}	mass of the equivalent 1dof system
M_{sh}	lumped shaker mass
m_e	rotating mass
n	soil porosity
p_w	pore water pressure
q_c	CPT cone resistance
R	lever arm
t	time
U	shaker displacement
u	soil displacement
$\bar{U}$	shaker steady-state displacement amplitude
$\bar{u}$	soil steady-state displacement amplitude
u_{inp}	bedrock steady-state displacement amplitude
u_{static}	static soil displacement
V_s	shear wave velocity
z	depth

REFERENCES

Angelides, D. C. & Roesset, J. M. (1981). Nonlinear lateral dynamic stiffness of piles. *Journal of Geotechnical and Geoenvironmental Engineering* **107**, No. ASCE 16635 Proceeding.

Anusic, I., Eiksund, G. R., Meissl, S. & Liingaard, M. A. (2017). Study of a new installation technique for large diameter monopiles. In *Proceedings of 19th International Conference on Soil Mechanics and Geotechnical Engineering (ICSMGE2017). Seoul, South Korea*, pp. 2261–2264.

Arany, L. & Bhattacharya, S. (2018). Simplified load estimation and sizing of suction anchors for spar buoy type floating offshore wind turbines. *Ocean Engineering* **159**, 348–357.

Archer, C., Simão, H., Kempton, W., Powell, W. & Dvorak, M. (2017). The challenge of integrating offshore wind power in the us electric grid. part i: Wind forecast error. *Renewable energy* **103**, 346–360.

Berger, E., Mahi, S. A., Pyke, R. *et al.* (1977). Simplified method for evaluating soil-pile-structure interaction effects. In *Offshore Technology Conference*, Offshore Technology Conference.

Bienen, B., Klinkvort, R. T., O'Loughlin, C., Zhu, F. & Byrne, B. (2018). Suction caissons in dense sand, part ii: vertical cyclic loading into tension. *Géotechnique* , 1–15.

Biot, M. (1956). Theory of elastic waves in a fluid-saturated porous solid. 1. low frequency range. *J. Acoust. Soc. Am.* **28**, 168–178.

BS EN (1991). 1-4: 2005 eurocode 1: Actions on structures - general actions - wind actions.

Byrne, B. W., Burd, H. J., Zdravkovic, L., Abadie, C. N., Houlsby, G. T., Jardine, R. J., Martin, C. M., McAdam, R. A., Pacheco Andrade, M., Pedro, A. M. *et al.* (2019). Pisa design methods for offshore wind turbine monopiles. In *Offshore Technology Conference*, Offshore Technology Conference.

Chan, A. H.-C. (1988). *A unified finite element solution to static and dynamic problems of geomechanics*. Ph.D. thesis, Swansea University.

Chancham, C., Waewsak, J. & Gagnon, Y. (2017). Offshore wind resource assessment and wind power plant optimization in the gulf of thailand. *Energy* **139**, 706–731.

Corciulo, S., Zanoli, O. & Pisanò, F. (2017). Transient response of offshore wind turbines on monopiles in sand: role of cyclic hydro–mechanical soil behaviour. *Computers and Geotechnics* **83**, 221–238.

Dobry, R. & Gazetas, G. (1988). Simple method for dynamic stiffness and damping of floating pile groups. *Geotechnique* **38**, No. 4, 557–574.

Doherty, P. & Gavin, K. (2012). Laterally loaded monopile design for offshore wind farms. *Proceedings of the Institution of Civil Engineers - Energy* **165**, No. 1, 7–17.

Dutch Ministry of Economic Affairs (2016). Energy report: transition to sustainable energy. *Technical report*, Ministry of Economic Affairs, The Netherlands, URL `https://www.government.nl/documents/reports/2016/04/28/energy-report-transition-tot-sustainable-energy`.

Elgamal, A., Yang, Z. & Parra, E. (2002). Computational modeling of cyclic mobility and post-liquefaction site response. *Soil Dynamics and Earthquake Engineering* **22**, No. 4, 259–271.

Fan, S., Bienen, B. & Randolph, M. F. (2019). Centrifuge study on effect of installation method on lateral response of monopiles in sand. *International Journal of Physical Modelling in Geotechnics* , 1–35.

Galavi, V., Beuth, L., Coelho, B. Z., Tehrani, F. S., Hölscher, P. & Van Tol, F. (2017). Numerical simulation of pile installation in saturated sand using material point method. *Procedia Engineering* **175**, 72–79.

Gazetas, G. (1983). Analysis of machine foundation vibrations: state of the art. *International Journal of Soil Dynamics and Earthquake Engineering* **2**, No. 1, 2–42.

Gazetas, G. & Dobry, R. (1984a). Horizontal response of piles in layered soils. *Journal of Geotechnical engineering* **110**, No. 1, 20–40.

Gazetas, G. & Dobry, R. (1984b). Simple radiation damping model for piles and footings. *Journal of Engineering Mechanics* **110**, No. 6, 937–956.

Graff, K. F. (2012). *Wave motion in elastic solids.* Courier Corporation.

Han, B., Zdravkovic, L. & Kontoe, S. (2016). Numerical and analytical investigation of compressional wave propagation in saturated soils. *Computers and Geotechnics* **75**, 93–102.

He, R., Kaynia, A. M. & Zhang, J. (2019). A poroelastic solution for dynamics of laterally loaded offshore monopiles. *Ocean Engineering* **179**, 337–350.

Houlsby, G., Kelly, R., Huxtable, J. & Byrne, B. (2005). Field trials of suction caissons in clay for offshore wind turbine foundations. *Géotechnique* **55**, No. 4, 287–296.

Houlsby, G., Kelly, R., Huxtable, J. & Byrne, B. (2006). Field trials of suction caissons in sand for offshore wind turbine foundations. *Géotechnique* **56**, No. 1, 3–10.

Hughes, T. J. R. (1987). *The finite element method: linear static and dynamic finite element analysis.* Prentice-Hall.

Kagawa, T. & Kraft, L. M. (1980). Lateral load-deflection relationships of piles subjected to dynamic loadings. *Soils and Foundations* **20**, No. 4, 19–36.

Kallehave, D., Byrne, B. W., LeBlanc Thilsted, C. & Mikkelsen, K. K. (2015). Optimization of monopiles for offshore wind turbines. *Philosophical Transactions of the Royal Society A: Mathematical, Physical and Engineering Sciences* **373**, No. 2035, 20140100.

Kallehave, D., Thilsted, C. L. & Liingaard, M. (2012). Modification of the API p-y formulation of initial stiffness of sand. In *Proceedings of Offshore Site Investigation and Geotechnics: Integrated Technologies - Present and Future. London, UK*, Society of Underwater Technology, pp. 465–472.

Kementzetzidis, E., Corciulo, S., Versteijlen, W. G. & Pisanò, F. (2019). Geotechnical aspects of offshore wind turbine dynamics from 3D non-linear soil-structure simulations. *Soil Dynamics and Earthquake Engineering* **120**, 181–199.

Kementzetzidis, E., Versteijlen, W. G., Nernheim, A. & Pisanò, F. (2018). 3D FE dynamic modelling of offshore wind turbines in sand: Natural frequency evolution in the pre-to after-storm transition. In *Numerical Methods in Geotechnical Engineering IX, Volume 2*, CRC Press, pp. 1477–1484.

Kontoe, S., Zdravkovic, L. & Potts, D. M. (2008). An assessment of time integration schemes for dynamic geotechnical problems. *Computers and geotechnics* **35**, No. 2, 253–264.

Kuhlemeyer, R. L. (1979). Static and dynamic laterally loaded floating piles. *Journal of Geotechnical and Geoenvironmental Engineering* **105**, No. ASCE 14394.

Liu, H. Y., Abell, J. A., Diambra, A. & Pisanò, F. (2019). Modelling the cyclic ratcheting of sands through memory-enhanced bounding surface plasticity. *Géotechnique* **69**, No. 9, 783–800.

Lysmer, J. & Kuhlemeyer, R. L. (1969). Finite dynamic model for infinite media. *Journal of the Engineering Mechanics Division* **95**, No. 4, 859–878.

Mattar, C. & Borvarán, D. (2016). Offshore wind power simulation by using wrf in the central coast of chile. *Renewable Energy* **94**, 22–31.

McGann, C. R., Arduino, P. & Mackenzie-Helnwein, P. (2015). A stabilized single-point finite element formulation for three-dimensional dynamic analysis of saturated soils. *Computers and Geotechnics* **66**, 126–141.

McKenna, F. T. (1997). *Object-oriented finite element programming: frameworks for analysis, algorithms and parallel computing.* Ph.D. thesis, University of California, Berkeley.

Mylonakis, G. & Gazetas, G. (1999). Lateral vibration and internal forces of grouped piles in layered soil. *Journal of Geotechnical and Geoenvironmental Engineering* **125**, No. 1, 16–25.

Newman, J. N. (1977). *Marine hydrodynamics.* MIT press.

Novak, M. (1974). Dynamic stiffness and damping of piles. *Canadian Geotechnical Journal* **11**, No. 4, 574–598.

Novak, M., Aboul-Ella, F. & Nogami, T. (1978). Dynamic soil reactions for plane strain case. *Journal of the Engineering Mechanics Division* **104**, No. 4, 953–959.

O'Rourke, M. J. & Dobry, R. (1982). Spring and dashpot coefficients for machine foundations on piles. *Special Publication* **78**, 177–198.

Paulsen, B. T., de Sonneville, B., van der Meulen, M. & Jacobsen, N. G. (2019). Probability of wave slamming and the magnitude of slamming loads on offshore wind turbine foundations. *Coastal Engineering* **143**, 76–95.

Pisanò, F. (2019). Input of advanced geotechnical modelling to the design of offshore wind turbine foundations. In *Proceedings of 17th European Conference on Soil Mechanics and Geotechnical Engineering (ECSMGE2019). Reykjavík, Iceland*, International Society of Soil Mechanics and Geotechnical Engineering (ISSMGE).

Pisanò, F. & Gavin, K. G. (2017). General report for TC209 - Offshore Geotechnics. In *Proceedings of 19th International Conference on Soil Mechanics and Geotechnical Engineering (ICSMGE2017). Seoul, South Korea.*

Pisanò, F. & Pastor, M. (2011). 1D wave propagation in saturated viscous geomaterials: improvement and validation of a fractional step Taylor–Galerkin finite element algorithm. *Computer methods in applied mechanics and engineering* **200**, No. 47-48, 3341–3357.

Shadlou, M. & Bhattacharya, S. (2014). Dynamic stiffness of pile in a layered elastic continuum. *Geotechnique* **64**, No. 4, 303.

Shadlou, M. & Bhattacharya, S. (2016). Dynamic stiffness of monopiles supporting offshore wind turbine generators. *Soil Dynamics and Earthquake Engineering* **88**, 15–32.

Skau, K. S., Page, A. M., Kaynia, A. M., Løvholt, F., Norén-Cosgriff, K., Sturm, H., Andersen, H., Nygard, T., Jostad, H. P., Eiksund, G. *et al.* (2018). REDWIN–REDucing cost in offshore WINd by integrated structural and geotechnical design. In *Journal of Physics: Conference Series*, vol. 1104, IOP Publishing, p. 012029.

Tehrani, F. S., Nguyen, P., Brinkgreve, R. B. & van Tol, A. F. (2016). Comparison of press-replace method and material point method for analysis of jacked piles. *Computers and Geotechnics* **78**, 38–53.

Tsai, Y.-C., Huang, Y.-F. & Yang, J.-T. (2016). Strategies for the development of offshore wind technology for far-east countries–a point of view from patent analysis. *Renewable and Sustainable Energy Reviews* **60**, 182–194.

Versteijlen, W. (2018). *Identification of effective 1D soil models for large-diameter offshore wind turbine foundations based on in-situ seismic measurements and 3D modelling.* Ph.D. thesis, Delft University of Technology.

Versteijlen, W., Renting, F., van der Valk, P., Bongers, J., van Dalen, K. & Metrikine, A. (2017a). Effective soil-stiffness validation: shaker excitation of an in-situ monopile foundation. *Soil Dynamics and Earthquake Engineering* **102**, 241 – 262, doi:https://doi.org/10.1016/j.soildyn.2017.08.003, URL `http://www.sciencedirect.com/science/article/pii/S0267726117301008`.

Versteijlen, W., Renting, F., van der Valk, P., Bongers, J., van Dalen, K. & Metrikine, A. (2017b). Effective soil-stiffness validation: Shaker excitation of an in-situ monopile foundation. *Soil Dynamics and Earthquake Engineering* **102**, 241–262.

Wang, X., Zeng, X., Li, J., Yang, X. & Wang, H. (2018). A review on recent advancements of substructures for offshore wind turbines. *Energy conversion and management* **158**, 103–119.

Watanabe, K., Pisanò, F. & Jeremić, B. (2017). Discretization effects in the finite element simulation of seismic waves in elastic and elastic-plastic media. *Engineering with Computers* **33**, No. 3, 519–545.

Zienkiewicz, O. C., Chan, A. H. C., Pastor, M., Schrefler, B. A. & Shiomi, T. (1999). *Computational geomechanics.* Wiley Chichester.

Zienkiewicz, O. C., Chang, C. T. & Bettess, P. (1980). Drained, undrained, consolidating and dynamic behaviour assumptions in soils. *Géotechnique* **30**, No. 4, 385–395.

APPENDIX

The dynamic response of a layered soil deposit has been studied throughout this work using a two-phase 3D FE model based on the well-known *u-p* formulation (Zienkiewicz *et al.*, 1999). Compared to its original conception (Zienkiewicz *et al.*, 1980), a simpler *u-p* formulation ('consolidation form') is adopted in the OpenSees FE software (Elgamal *et al.*, 2002), so that fluid inertial terms (not only soil-fluid relative accelerations) are completely neglected (Chan, 1988). Using the same two-phase FE model, both drained and undrained conditions have been analysed by setting, respectively, very high or very low values of soil permeability. Obviously, a simpler one-phase model could be adopted for uncoupled drained analyses, as long as the saturated soil-fluid mass density is set to represent an underwater soil deposit.

3D one-phase and two-phase dynamic equations are compared in Table A1 (Equations (A1)-(A4)), where ρ indicates the mass density of fluid-saturated soil, and $1/Q = n/K_f + (1-n)/K_s$ the overall compressibility of solid and fluid constituents (average of the corresponding bulk moduli, K_f and K_s, weighted on the porosity n) – all symbols are defined in the notation list. It is readily apparent that, if elastic, stress-independent behaviour is considered for the soil skeleton, then the *u-p*/consolidation model reduces exactly to the one-phase/drained model as the soil permeability k' tends to infinity. It should be noted that, in the dynamic version of the Darcy law, the hydraulic conductivity k' ([length]^3[time]/[mass]) is introduced in the relationship between (relative) discharge velocity and pore pressure gradient (instead of the hydraulic head gradient). The more usual permeability coefficient k ([length/time]) can be obtained as $k = k'\rho_f g$, where ρ_f and g stand for fluid density and gravity acceleration, respectively (Zienkiewicz *et al.*, 1999).

The same conclusion is further corroborated in Table A1 (Equations (A5)-(A7)) for the case of a 1D elastic soil column under forced harmonic motion. The steady-state eigenvalue problems associated with (A5), both one-phase and two-phase/incompressible, are formulated in (A6) and solved for the following boundary conditions: (i) free surface at the top, (ii) rigid/impervious bedrock at $y = H$, (iii) imposed harmonic motion at the bedrock, $u\left(H,t\right) = u_{inp}\left(\Omega\right)\exp\left(i\Omega t\right)$, with the amplitude u_{inp} possibly a function of the input circular frequency Ω. The two-phase eigenfunction $\bar{u}$ tends to its one-phase counterpart as $k' \rightarrow \infty$ (further details about the 1D two-phase solution available in Pisanò & Pastor (2011)), which re-confirms the legitimacy of using a *u-p*/consolidation model to recover fully drained conditions as a special case.

Governing Equations	one-phase	two-phase	
mixture momentum balance	$\rho\ddot{u}_i = \sigma_{ij,j}$	$\rho\ddot{u}_i = \sigma_{ij,j} = \sigma'_{ij,j} - p_{w,i}$	(A1)
elastic stress-strain law	$\sigma_{ij} = \frac{1}{2}D_{ijkl}\left(u_{k,l} + u_{l,k}\right)$	$\sigma'_{ij} = \frac{1}{2}D_{ijkl}\left(u_{k,l} + u_{l,k}\right)$	(A2)
balance of fluid momentum and mass + Darcy law	—	$k' p_{w,ii} = \dot{u}_{i,i} + \frac{\dot{p}_w}{Q}$	(A3)
Combined form (A1)+(A2)+(A3)	$\rho\ddot{u}_{i,i} = \frac{1}{2}\left[D_{ijkl}\left(u_{k,l} + u_{l,k}\right)\right]_{,ji}$	$\rho\ddot{u}_{i,i} = \frac{1}{2}\left[D_{ijkl}\left(u_{k,l} + u_{l,k}\right)\right]_{,ji} - \frac{\dot{u}_{i,i} + \dot{p}_w/Q}{k'}$	(A4)
1D elastic soil column under harmonic excitation			
1D governing equation	$\ddot{u} - \frac{\bar{E}}{\rho}u_{,yy} = 0$	$\left[\ddot{u} - \frac{\bar{E}}{\rho}u_{,yy} + \frac{1}{k'\rho}\left(1 + \frac{\bar{E}}{Q}\right)\dot{u}\right]_{,yy} - \frac{1}{Qk'}\dddot{u} = 0$	(A5)
eigenvalue problem $(Q \to \infty)$	$\bar{u}_{,yy} + \frac{\rho\Omega^2}{\bar{E}}\bar{u} = 0$	$\left[\bar{u}_{,yy} + \left(\frac{\rho\Omega^2}{\bar{E}} - \frac{\Omega}{k'\bar{E}}i\right)\bar{u}\right]_{,yy} = 0$	(A6)
eigenfunction $\bar{u}$(y,Ω) $(Q \to \infty)$	$\frac{\cos\left(\sqrt{\frac{\Omega^2\rho}{\bar{E}}}y\right)}{\cos\left(\sqrt{\frac{\Omega^2\rho}{\bar{E}}}H\right)}u_{inp}(\Omega)$	$\frac{\cos\left(\sqrt{\frac{\Omega^2\rho}{\bar{E}} - \frac{\Omega}{k'\bar{E}}i}\;y\right)}{\cos\left(\sqrt{\frac{\Omega^2\rho}{\bar{E}} - \frac{\Omega}{k'\bar{E}}i}\;H\right)}u_{inp}(\Omega)$	(A7)

Table A1. Dynamic soil modelling: 1-phase vs 2-phase (*u-p*/consolidation) formulations. Notation/conventions: (i) index notation for space derivatives, dots used for time differentiation; (ii) total and effective stresses denoted by σ_{ij} and σ'_{ij}, respectively; (iii) opposite sign conventions adopted for solid stresses (positive if tensile) and pore pressure (positive if compressive); (iv) the incompressible limit $(Q \to \infty)$ is considered in (A6)-(A7) with no loss of generality.

Frequency effects in the dynamic lateral stiffness of monopiles in sand: insight from field tests and 3D FE modelling

June 9, 2020

E. Kementzetzidis – TU Delft (The Netherlands)
A.V. Metrikine – TU Delft (The Netherlands)
W.G. Versteijlen – Siemens Gamesa (The Netherlands)
F. Pisanò – TU Delft (The Netherlands)

Response to Assessor

Many thanks for this positive final assessment, and for proposing useful changes that improved the overall quality of the manuscript. We implemented most textual changes as suggested, with only a very few adapted to our personal taste. For a faster final check, modified sentences are highlighted in blue in the revised manuscript following this response letter. Figures 1,2,3,4,12 were also modified to improve clarity/readability as recommended. Once again, we are very grateful for the constructive review process.

Géotechnique **00**, 1–15 [http://dx.doi.org/10.1680/geot.XX.XXXXX]

Frequency effects in the dynamic lateral stiffness of monopiles in sand: insight from field tests and 3D FE modelling

E. KEMENTZETZIDIS*, A.V. METRIKINE*, W.G. VERSTEIJLEN†, F. PISANÒ*

With the offshore wind industry rapidly expanding worldwide, geotechnical research is being devoted to foundation optimisation – most intensively for large-diameter monopiles. The analysis and design of monopiles still suffers from significant uncertainties in relation to cyclic/dynamic loading conditions. This work aims to shed new light on dynamic soil-monopile interaction, based on the results of unique full-scale experiments performed at the Westermeerwind wind park (Netherlands). The response of a 24 m long, 5 m diameter monopile to harmonic lateral loading of varying amplitude and frequency is inspected. The analysis of original field measurements (soil accelerations and pore pressures) enables to link the lateral stiffness observed at the monopile head to dynamic effects occurring in the surrounding soil. The interpretation of measured data is supported by three-dimensional finite element studies, also looking at the influence of drainage conditions and monopile size. The set of results presented supports the need for dynamics-based monopile design as higher frequencies gain relevance in most recent offshore wind developments.

KEYWORDS: piles & piling, sands, dynamics, full-scale tests, soil-structure interaction, finite-element modelling

INTRODUCTION

In recent years renewable energy resources have gained increasing relevance worldwide in the fight against climate change, in order to free human development from polluting fossil fuels. For example in the Netherlands, the Ministry of Economic Affairs has recently drawn a roadmap for CO2-neutral energy supply by 2050 (Dutch Ministry of Economic Affairs, 2016). The transition to renewables is regarded as one of the pillars for achieving CO_2-neutrality, a goal towards which public agencies, industry and academia, are currently collaborating.

The boom of the offshore wind market is continuing in Northern Europe and gradually expanding to other continents (Tsai *et al.*, 2016; Mattar & Borvarán, 2016; Archer *et al.*, 2017; Chancham *et al.*, 2017). Technological improvements have enabled the growth in size and capacity of offshore wind turbines (OWTs), along with remarkable cost reduction – notable examples of new-generation OWTs are General Electric's Haliade-X 12 MW and Siemens Gamesa's 14 MW turbines, featuring a rotor diameter of 220 m and 222 m, respectively. The trend towards installations in deeper waters and harsher environments poses significant technical challenges, especially regarding support structures and foundations (Pisanò & Gavin, 2017; Versteijlen, 2018). To date, about 80% of all OWTs installed in Europe are founded on monopiles, tubular steel piles of large diameter. Although alternative structural concepts are also receiving attention (e.g., jacket-supported or floating OWTs – Wang *et al.* (2018); Bienen *et al.* (2018); Arany & Bhattacharya (2018)), monopile-supported OWTs will continue to dominate the market in the foreseeable future as a low-risk solution (Kallehave *et al.*, 2015).

The uncertainties still associated with monopile design (Doherty & Gavin, 2012; Kallehave *et al.*, 2012) have given rise to valuable research projects, such as PISA in the UK (Byrne *et al.*, 2019), REDWIN in Norway (Skau *et al.*, 2018) and, in the Netherlands, DISSTINCT (Versteijlen *et al.*, 2017a). One of the main open questions in monopile design concerns the effects of installation on the operational performance. At present, most monopiles are driven into the soil by impact hammering, a method believed to highly influence the state of the soil around the monopile shaft and under the tip. Interesting steps towards quantifying installation effects have been recently taken (Tehrani *et al.*, 2016; Anusic *et al.*, 2017; Galavi *et al.*, 2017; Fan *et al.*, 2019), although with no wide consensus about long-term consequences. The above-mentioned DISSTINCT project used dynamic load tests on a full-scale, impact-driven monopile to address a number of interrelated questions (Versteijlen *et al.*, 2017b): are (pre-installation) soil properties from site investigation relevant to (post-installation) soil-monopile interaction? Are existing prediction models adequate to capture such interaction as it occurs in the field? Would field tests on a single monopile provide sufficient insight into real dynamic behaviour, and enable cost optimisation at the wind park scale?

In the past decades, a number of authors have studied the dynamic interaction between soil and (slender) piles, originally in relation to vibrating machines, bridge piers, and earthquakes (Novak, 1974; Kuhlemeyer, 1979; Kagawa & Kraft, 1980; Angelides & Roesset, 1981; Dobry & Gazetas, 1988; Gazetas & Dobry, 1984a; Mylonakis & Gazetas, 1999; Shadlou & Bhattacharya, 2014). More recently, contributions about short monopiles and caissons for OWTs have also appeared in the literature (Houlsby *et al.*, 2005, 2006; Shadlou & Bhattacharya, 2016; He *et al.*, 2019). DISSTINCT added to this research thread through a field investigation on monopile behaviour under loading frequencies larger than currently considered in offshore design. Indeed, the range of relevant loading frequencies is gradually expanding beyond 0.5 Hz, mostly due to OWTs being built in seismically active regions, and/or exposed to

---

Manuscript received...

* Faculty of Civil Engineering and Geosciences, Delft University of Technology, Stevinweg 1, 2628 CN Delft (The Netherlands)
† Siemens Gamesa Renewable Energy, Prinses Beatrixlaan 800, 2595 BN, Den Haag (The Netherlands)

'breaking & slamming' sea waves in deeper waters (Paulsen *et al.*, 2019). This paper reviews full scale field test results (DISSTINCT) with support from three-dimensional (3D) finite element (FE) modelling (Pisanò, 2019). Focus is on the frequency-dependence of the lateral monopile stiffness as observed in the field during low-amplitude vibrations. Field data and numerical simulation results are critically compared to explore the role of relevant dynamic effects, such as structural resonance(s) in the embedded monopile and pore pressure variations in the surrounding soil.

FULL-SCALE FIELD TESTS

The present work builds on the results of full-scale field tests performed in the framework of DISSTINCT (*Dynamic Interaction between Soil & Structures, Tools & Investigations using Numerical Calculation & Testing*), a 4-years collaborative project (2014-2018) involving TU Delft, Siemens Gamesa Renewable Energy, DNG-GL, Fugro, SWP and MBO Offshore. Methodology and main outcomes of the experimental programme are briefly outlined in this section, while more details can be found in Versteijlen *et al.* (2017b) and Versteijlen (2018).

Dynamic load tests were executed on a monopile at the Westermeerwind wind farm, located in the Netherlands on the eastern shore of the IJsselmeer lake (Figure 1). The monopile was 5 m in diameter and embedded under water in prevalently sandy soil for 24.05 m (L_{emb}) of its length ($L = 33.9$ m) – Figures 2–3.

Fig. 1. Location of the Westermeerwind wind farm (square).

Site characterisation

The wind farm site was characterised by combining seismic cone penetration tests (SCPTs) and boreholes. Within the shallowest 30 m (cf. to $L_{emb} = 24.05$ m), in situ tests confirmed the presence of medium-dense to dense sand ($D_R \approx 60 - 85\%$), with interleaved thin layers of peat and stiff clay at about 1 m and 20 m depth below the mudline, respectively – see Figure 2 regarding the SCPT45 test performed at the monopile location shown in Figure 1. Additional information about soil permeability at the site was inferred by the results of two HPT-CPTs (Hydraulic Profiling Tests) and one slug test executed near the monopile. The results of these tests returned a continuous permeability profile, featuring average sand permeability of approximately 1.4×10^{-4} m/s.

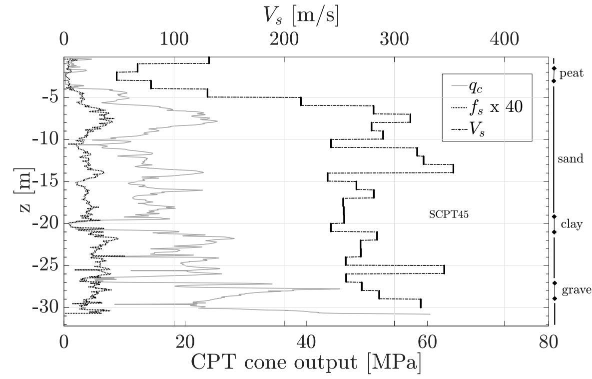

Fig. 2. Site characterisation near the monopile location based on SCPT tests and borehole data (right side, straight line denotes presence of sand) – q_c: cone resistance, f_s: sleeve friction, V_s: shear wave velocity. Modified after Versteijlen *et al.* (2017b).

At the IJsselmeer lake the Appelscha geological formation is known to create a rigid bedrock at depths ranging from 60 to 100 m. This information enables estimation of the multiple resonance frequencies associated with vertical shear wave propagation:

$$f_n = \frac{(2n-1)V_s}{4H} \tag{1}$$

where the n^{th} resonance frequency depends on the shear wave velocity V_s and the bedrock depth H. Inferring from Figure 2 a representative V_s of 300 m/s, the first resonance of the sandy deposit is expected to lie in the range between 0.75 and 1.25 Hz (Versteijlen *et al.*, 2017b).

Field testing procedures and measurements

After impact pile driving, dynamic lateral load tests were executed by placing a vibratory device at the top of the monopile as depicted in Figure 3 – a shaker consisting of two hydraulically powered large cogwheels. The shaker was able to deliver a maximum hydraulic power of 50 kW and rotate at a maximum frequency of 8.6 Hz. Steel plates were attached over the cogwheels at varying radial distance, and three different weight setups were considered to study the influence of the loading amplitude. Detailed studies delivered accurate estimates of effective lever arm (R) and rotating mass (m_e) associated with each set-up (Versteijlen, 2018). The total force $F(t)$ applied to the monopile head can thus be calculated as a function of the angular frequency of mass rotation (Ω, [rad/s]):

$$F(t) = m_e \Omega^2 R \sin(\Omega t) \tag{2}$$

where t denotes time. Different load cases were set up, and of particularly relevance to this paper were those involving a step-wise increase in excitation frequency. For each mass configuration, the duration of each frequency step was deemed sufficient to approach steady-state conditions. Three steel plates of different mass were used to generate the experimental scenarios summarised in Table 1. It was also evaluated that DISSTINCT shaking tests loaded the pile with forces much lower than those to be later transmitted by the installed OWT, and therefore well below the lateral capacity of the foundation.

Setup	$m_e \times R$ [mkg]	Frequency range [Hz]	Force range [kN]
Heavy weight	239.32	1.04 - 4.03	10.31 - 153.42
Middle weight	88.76	1.06 - 6.70	3.95 - 157.31
Light weight	32.08	5.04 - 8.68	32.15 - 95.40

Table 1. Technical specifications for the DISSTINCT load cases considered in this study.

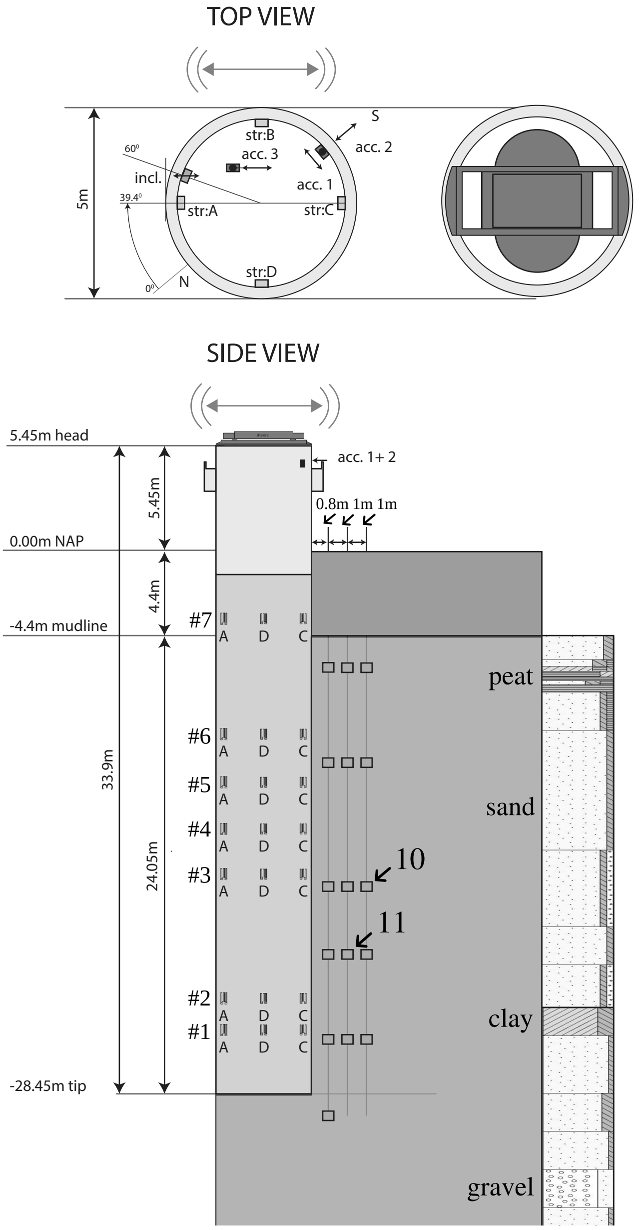

Fig. 3. Measurement setup. Depth values correspond with the NAP (Dutch equivalent of Mean Sea Level). Square markers in the soil region indicate locations of soil sensors, i.e. cones equipped with accelerometers and pore water transducers. Numbering along the pile (e.g. #1, #2, etc.) refers to arrays of strain gauges. Structural accelerations were measured both at the pile head and at the shaker. The locations of pore water and soil acceleration sensors 10 and 11 Arrows indicate the locations of pore pressure and acceleration sensors 10 and 11 in the soil – modified after Versteijlen *et al.* (2017b).

As illustrated in Figure 3, the response of the monopile was recorded through sensors installed on the pile and in the soil (Versteijlen *et al.*, 2017b; Versteijlen, 2018). Two Althen AAA320 accelerometers where placed on the pile head and one on the shaker, together with strain gauges along the monopile shaft. The soil response around the pile was detected by measuring local accelerations and variations in pore water pressure. The soil motion was recorded via 16 AS28/5g accelerometers capable of measuring accelerations lower than 1 gal. Variations in pore water pressure were recorded by means of fully analogue, 4-20 mA pressure transmitters of ATM/N type, endowed with a Wheatstone bridge circuit with analogue amplifier. It was thus possible to detect ‘practically infinitesimal’ pore pressure variations (very high resolution), and record maximum values up to 500 kPa with a deviation no larger than 0.3 kPa.

Experimental data

The analyses presented in this work are mainly based on acceleration data at the shaker and pore water pressure variations in the soil. Acceleration and pore pressure signals were post-processed by first removing their baseline (mean value), and then low-pass filtering at 10 Hz against high-frequency noise. All recorded data were interpreted by assuming the soil-monopile system to behave as a damped linear system at steady state for each frequency step. While the assumption of linearity was suggested by the weak loading amplitudes in Table 1, the attainment of stationary conditions in each frequency step was supported by good agreement with numerical simulation results based on the same assumption – see later. Overall, assuming steady-state linear response also justified the above-mentioned low-pass filtering of acceleration records. As free-vibration components would be eventually damped out, it seemed appropriate to focus on a relatively narrow frequency band around the main input spectrum (Table 1), so as to exclude most of the noise in sensor records. Filtered acceleration signals from the shaker and varying mass rotation frequency (henceforth, ‘loading frequency’) are illustrated in Figure 4 for the three test setups in Table 1.

As (linear) steady state theoretically implies vibrations at the same frequency Ω of the loading (Equation 2), it was possible to relate monoharmonic amplitudes of applied force $F(\Omega)$ and shaker displacement amplitudes ($\bar{U}$) from recorded data, with the latter obtained from acceleration amplitudes ($\ddot{\bar{U}}$) as:

$$\bar{U}(\Omega) = -\frac{\ddot{\bar{U}}(\Omega)}{\Omega^2} \tag{3}$$

Figure 5 illustrates (steady-state) relationships between applied forces and displacement amplitudes for the three loading scenarios (heavy, middle, light) – with frequency-dependence implicitly embedded into data points. The same data in Figure 5 are alternatively plotted in Figure 6a in terms of absolute value of the lateral dynamic stiffness ($|K_{dyn}|$) against the loading frequency. Data-based $|K_{dyn}|$ values were obtained as the ratio between the amplitudes of applied force and displacement at steady state.

The comparison between Figures 5 and 6a hints that, under the low loads considered (Table 1), the excitation

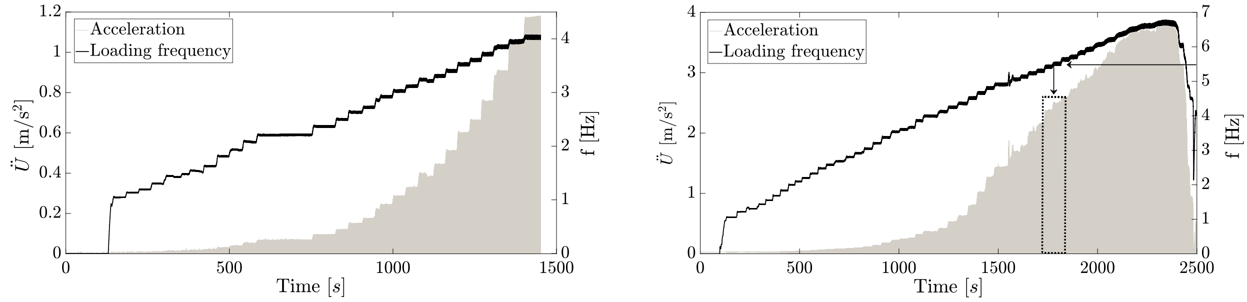

(a) Heavy weight **(b) Middle weight**

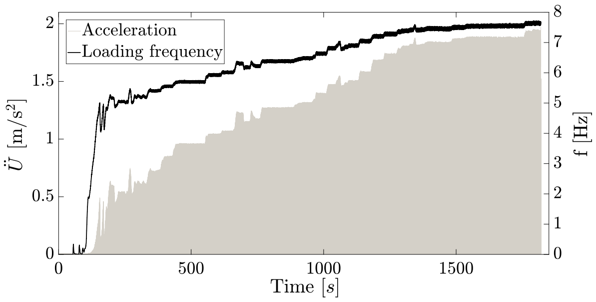

(c) Light weight

Fig. 4. Time evolution of accelerations ($\ddot{U}$) recorded at the shaker and loading frequency (f) for the three loading scenarios in Table 1. Only the positive side of acceleration diagrams are plotted for clarity. The dashed window in (b) highlights the response around 5.5 Hz.

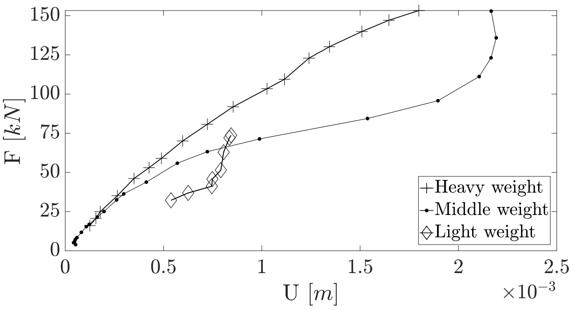

Fig. 5. Steady-state relationship between amplitude of the applied force (F) and displacement (U) at the shaker for the three loading scenarios in Table 1.

frequency impacts the pile lateral stiffness in a more profound manner than the loading amplitude. The dynamic pile head stiffness in Figure 6a appears clearly frequency-dependent, with a drop in $|K_{dyn}|$ of about 285% observed between 1-2 Hz and 5.3 Hz. As shown in Figure 6b, experimental data were then re-interpreted as if they resulted from a one degree-of-freedom (1dof) mass-damper-spring oscillator, featuring (static) stiffness, mass and damping coefficient equal to $K_0^{1dof} = 160$ MN/m, $M^{1dof} = 134$ tons and $C^{1dof} = 1.482$ tons$\cdot s^{-1}$, respectively. Such settings in the equivalent 1dof system are associated with a resonance frequency of 5.5 Hz and a damping ratio $\zeta^{1dof} = 16\%$, whereas the absolute value of the 1dof dynamic stiffness $|K_{dyn}^{1dof}|$ was derived from the absolute value of the frequency response function $G(\Omega) = U(\Omega)/F(\Omega)$:

$$
\begin{aligned}
&|K(\Omega)_{dyn}^{1dof}| = 1/|G(\Omega)| = \\
&= \sqrt{(K_0^{1dof} - M^{1dof}\Omega^2)^2 + (C^{1dof}\Omega)^2}
\end{aligned}
\tag{4}
$$

and then used to match the reduction in dynamic stiffness observed in experimental $|K_{dyn}|$ trends. The associated 1dof damping ratio of 16% may not be solely attributed to energy dissipation in the soil: generally, input energy will be dissipated through several physical mechanisms, including material damping (in the soil and in the monopile) as well as wave radiation. It should also be noted that 1dof fitting is fully adequate up to its resonance frequency, while $|K_{dyn}|$ is clearly over-predicted beyond that point. The physical nature of such resonance is discussed later on.

Interpretation of strain gauge data

Data from the strain gauges along the monopile supported the interpretation of the structural response during all shaking tests. For example, Figure 7 reports 2 seconds of axial strains associated with the middle weight setup towards the end of the 5.5 Hz frequency step – the frequency at which the lowest $|K_{dyn}|$ is observed. Same as for the acceleration signals, strain data were also low-pass filtered at 10 Hz and corrected for mean offset. The strain time histories in Figure 7 relate to sensors from 2A to 7A (Figure 3). The highest pile bending moment is expected to occur where the highest axial strain is recorded, i.e. at sensor 6A. Importantly, all strain gauges recorded at 5.5 Hz simultaneous compression and extension along the same side of the monopile, meaning that the stiffness degradation in the $|K_{dyn}|$ frequency-dependence is associated with the first bending mode.

Assessment of soil measurements

As previously mentioned, an array of accelerometers and pore-pressure sensors were installed in the soil near the monopile. As for pore pressure measurements, most attention was devoted to transient variations (Δp_w) with respect to pre-shaking, hydrostatic values. Generally, low

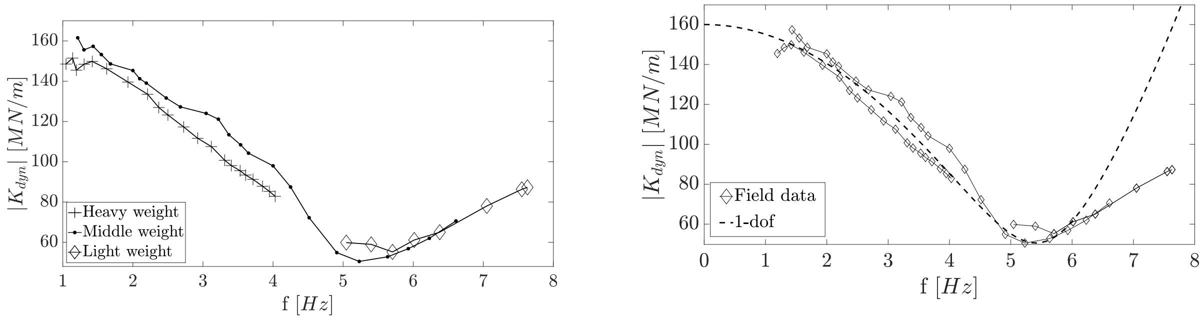

(a) from post-processing of field data for the three loading scenarios in Table 1.

(b) 1dof fitting of field data – static stiffness: K_0^{1dof} =160 MN/m, damping: $\zeta^{1dof} = 16\%$, resonance frequency: f_{res}=5.56 Hz.

Fig. 6. Frequency-dependence of the dynamic lateral stiffness $|K_{dyn}|$ observed at the monopile head.

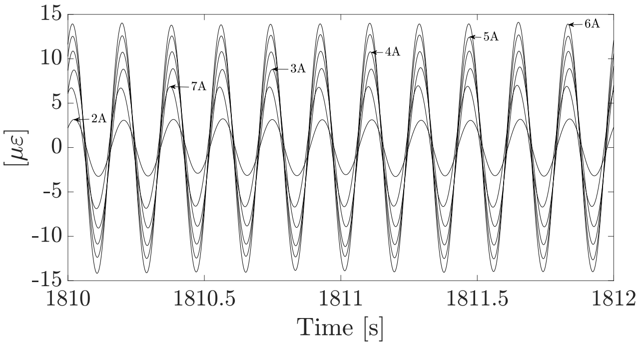

Fig. 7. Axial strains (ϵ) recorded along the monopile for the middle weight setup at the loading frequency of 5.5 Hz.

levels of soil acceleration ($\ddot{u}$) and pore pressure variations were recorded for the low-amplitude loads applied by the shaker, in the order of 0.1-0.2 m/s^2 and 0.5 kPa, respectively. Only pore pressure measurements in strong correlation with pile shaking were considered after selection based on the following procedure:

1. both soil acceleration and pore pressure signals were low-pass filtered at 10 Hz (see Figures 8a-8b), then normalised with respect to their maxima;
2. cross-correlation functions were numerically determined for pairs of (normalised) acceleration and pore pressure signals, so as to objectively quantify signal similarity;
3. only pore pressure measurements highly correlated with soil motion were deemed reliable.

The above procedure led to ‘approve’ only those sensors ensuring high cross-correlation between pore pressure variation and acceleration. For the middle weight setup taken as main reference, this prerequisite was only fulfilled by sensors 10 and 11 in Figure 3. For both sensors, correlations between pore pressure variations and horizontal accelerations were very similar regardless of the direction (x or y) – the cross-correlations shown in Figure 8 relate to measured accelerations projected along the loading direction.

3D FE MODELLING

3D FE analysis is proving increasingly valuable to modern offshore wind developments, in that it can support the understanding of complex geotechnical mechanisms, as well as the conception of engineering design methods (Kementzetzidis *et al.*, 2018, 2019; Pisanò, 2019; Byrne *et al.*, 2019). 3D FE modelling was carried out through the OpenSees simulation platform (McKenna, 1997), however with no need for advanced, non-linear modelling of soil behaviour. As DISSTINCT field tests were performed by applying low-amplitude vibrations, the soil was idealised as a water-saturated, linear elastic, porous medium, with hydro-mechanical coupling effects possibly taking place depending on well-known governing factors (Zienkiewicz *et al.*, 1999).

Numerical studies were conducted at two levels, aiming to investigate the response of soil-monopile system as a whole, but also the dynamics of the site prior to pile installation (‘soil-only’ analyses). The following three types of FE dynamic analyses were performed:

- soil deposit subjected to harmonic horizontal loading at the free surface;
- soil deposit subjected to harmonic vertical loading at the free surface;
- soil-monopile system subjected to harmonic horizontal loading at the monopile head as during the reference shaking tests.

In all cases sinusoidal point loads were applied until the attainment of steady state (total duration up to 120 seconds in some cases), with loading frequency ranging from 0 to 7.5 Hz and load application point shown in Figure 10.

Governing equations and space/time discretisation

The 3D FE model was built on the Biot-Zienkiewicz u-p coupled formulation described in Zienkiewicz *et al.* (1980), particularly in the simplified ‘consolidation form’ studied by Chan (1988). Such formulation enabled analysis of the extreme hydromechanical bounds of fully drained and undrained response with a single model, by setting either very high or very low soil permeability in the coupled FE model. As shown in the Appendix, a u-p model of the form referred to, produces results that are equivalent to the outcome of a one-phase/drained model as the permeability tends to infinity (i.e., to very high values). Given the assumption of linear elastic behaviour, the properties of the soil skeleton were directly inferred from site investigation data (SCPT45, Figure 2) to characterise the stratigraphy shown in Figure 9. The typical value of $K_f = 2.2 \cdot 10^6$ kPa was assigned to the bulk modulus of the pore water. The

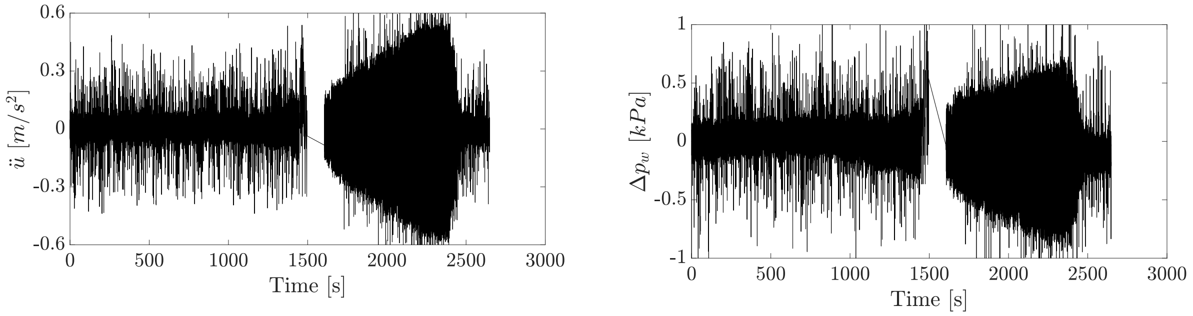

(a) filtered acceleration ($\ddot{u}$) (baseline removed) at sensor 10.

(b) filtered pore pressure variation Δp_w at sensor 10.

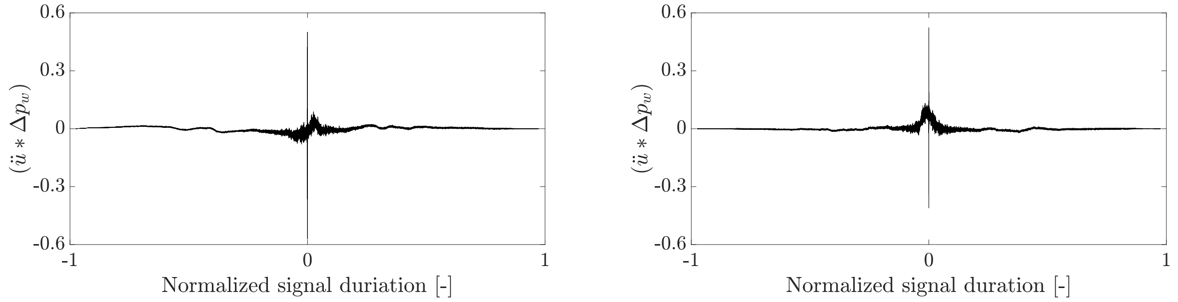

(c) acceleration-pressure cross-correlation for sensor 10.

(d) acceleration-pressure cross-correlation for sensor 11.

Fig. 8. Comparative assessment of soil acceleration and pore pressure variation data for the middle weight load setup in Table 1. Data gaps in (a) and (b) around 1500 s were caused by partial corruption of original data files. (c) & (d) show the cross-correlation between acceleration-pore water pressure signals ($\ddot{u} * \Delta p_w$) for sensors 10 and 11.

geometrical/loading symmetry of the problem was exploited to build a less expensive half-model.

The soil domain was discretised using the eight-node H1-P1ssp stabilised elements developed by McGann *et al.* (2015), featuring equal-order, linear interpolation of both displacement and pore pressure unknowns. The benefits of H1-P1ssp elements in relation to soil-monopile simulations are described by Corciulo *et al.* (2017), and include the stabilisation of pore pressure instabilities as undrained conditions are approached. Space discretisation was set to ensure appropriate propagation of harmonics up to 8 Hz, so that no less than 7–8 elements per wavelength were guaranteed in that frequency range. The standard Newmark integration algorithm was selected for time stepping, with integration parameters β and γ equal to 0.6 and 0.3025, respectively (Hughes, 1987). A time-step size of $\Delta t = 8.3 \times 10^{-4} s$ was found appropriate after numerical sensitivity studies (Watanabe *et al.*, 2017) – not reported for brevity.

To alleviate computational costs, it was not attempted to model the real location of the bedrock at the IJsselmeer lake, about 100 m below the mudline. This choice was noted to affect the simulated dynamics of the soil deposit (and in turn of soil-monopile interaction), however with no serious impact on the general conclusions drawn later on in this study.

Structural modelling of shaker and monopile

The embedded portion of the monopile was modelled as a 3D steel continuum and discretised by means of one-phase, eight-node ssp bricks (McGann *et al.*, 2015). Conversely, the above-mudline part was modelled as an elastic beam and discretised through twenty Timoshenko beam elements ($\approx$ 50 cm each), featuring consistent (non-diagonal) mass matrix. The mass of the shaker M_{sh} was lumped at the top of the monopile – see Figure 10. Added mass effects associated with surrounding sea water were simplistically introduced in the form of nodal lumped masses evenly distributed along the water depth $H_w \approx 4.5$m (Figure 3), and calculated as twice the water mass in the submerged OWT volume (Newman, 1977).

The soil model use here was relatively simplistic in that it was not designed to capture installation effects or the non-linear frictional behaviour of the soil-pile interface. Although it is clearly unrealistic to assume perfect soil-pile bonding, this choice allowed to preserve the intended linearity of the analyses, and avoided the assumption of input parameters which are not based upon specific soil characterisation. It was noticed, however, that interface properties may quantitatively affect dynamic soil-monopile interaction, especially at higher frequencies – this matter will receive further attention in future studies.

Energy dissipation in the numerical model

Energy dissipation (damping) plays an essential role in dynamic soil-structure interaction. OWTs dissipate energy during operations in multiple ways, such as:

- aerodynamic damping due to interaction between wind and rotating blades;
- hydrodynamic damping associated with monopile-water interaction;
- damping in structural materials (steel) and connections;
- damping in the soil arising from material dissipation, hydro-mechanical effects and wave radiation – see also Kementzetzidis *et al.* (2019).

In all FE simulations, aerodynamic and hydrodynamic damping were neglected, since no actual OWT tower was

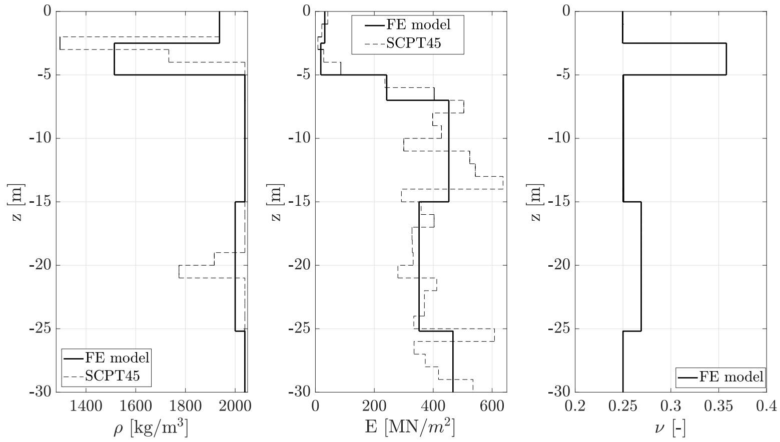

Fig. 9. Depth (z) profiles of saturated mass density (ρ) and elastic properties, Young's modulus (E) and Poisson's ratio ν, adopted in FE simulations.

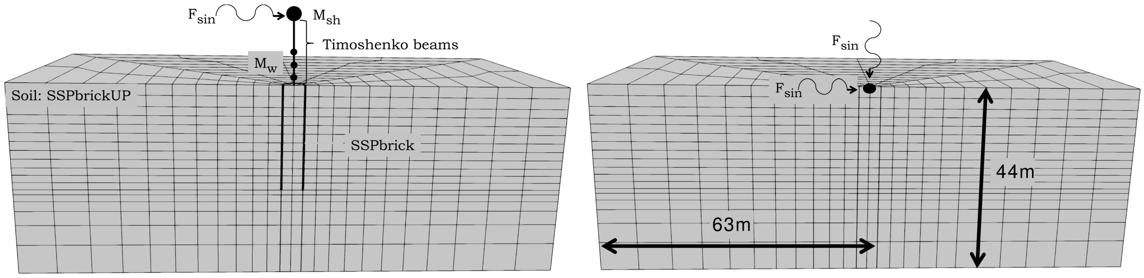

(a) shaker-monopile-soil

(b) soil-only

Fig. 10. Discretised soil domain and loading settings in complete and 'soil-only' FE analyses.

present during the field tests in very shallow water depth (only 4.4 m above the mudline). It is also worth mentioning that:

- wave radiation through lateral domain boundaries was enabled based on the well-established approach by Lysmer & Kuhlemeyer (1969);
- with the soil modelled as a linear elastic material, no damping in the solid skeleton was accounted for, in reasonable agreement with the small amplitude vibrations associated with the load cases in Table 1. The use of Rayleigh damping to model dissipation in the soil skeleton at very small strains was not pursued, due to the lack of relevant data for calibration;
- (compressional) wave motion in saturated porous media is generally dissipative due to hydro-mechanical coupling effects – for instance, under the fully undrained conditions considered later on (Biot, 1956; Han *et al.*, 2016);
- steel damping in the monopile was introduced according to Eurocode 1 BS EN (1991), with (Rayleigh) damping ratio $\zeta_{steel} = 0.19\%$ at the pivotal frequencies of 0.1 and 80 Hz;
- numerical damping spontaneously arises from Newmark's time integration algorithm set up as mentioned above. Nonetheless, algorithmic dissipation proved beneficial in attenuating high-frequency spurious oscillations in the simulated response (Kontoe *et al.*, 2008).

FE-BASED INTERPRETATION OF FIELD DATA

This section elaborates on the interpretation of field observations based on 3D FE results.

'Soil-only' simulations

Preliminary 'soil-only' simulations were performed to investigate the dynamics of the reduced soil model, and quantify its influence on the response of the shaker-monopile-soil system. The layered soil domain was subjected to mono-harmonic loading, either horizontal or vertical (Figure 10), spanning the frequency range of interest from 0 Hz (static loading) to 8 Hz. Hydro-mechanical coupling effects were inhibited by setting an unrealistically high soil permeability of 10^6 m/s, i.e., sufficiently large to make the water-saturated soil behave as a one-phase porous medium of identical total mass density – see Appendix. Horizontal/vertical soil responses at steady state are illustrated in Figure 11 in terms of amplification factors $A = |\bar{u}_{dyn}|/u_{static}$ at the shaker location, and phase differences between applied load and predicted soil displacement – u_{static} represents the displacement computed under a static load of magnitude equal to the amplitude of the dynamic load.

Phase difference trends in Figure 11b show in-phase force-displacement oscillations until about 2.5 Hz and 4.5 Hz for horizontal and vertical loading, respectively. As is well-known, nil phase difference is indicative of a quasi-static response with no waves propagating in the domain. The frequencies numerically identified (2.5 Hz and 4.5 Hz) are usually referred to as 'cut-off' frequencies, and mark the transition from 'evanescent waves' (vibrations exponentially

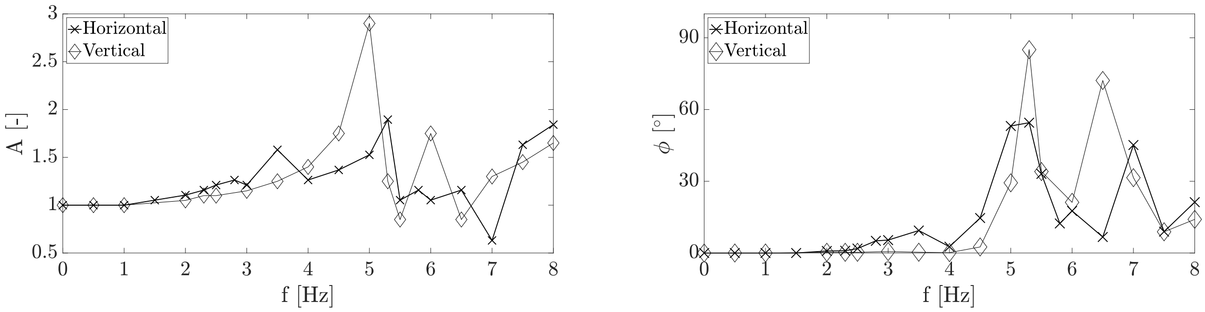

(a) Amplification factor (A) **(b) Phase difference (ϕ)**

Fig. 11. Simulated steady-state responses of the soil deposit to horizontal and vertical point loading at varying loading frequency (f).

decaying along the distance from the source) to actual wave motion (Graff, 2012). Overcoming the cut-off frequency also determines the onset of radiation damping, primary source of energy dissipation in the FE soil models set up in this work. Previous studies on radiation damping in 3D continua pointed out its dependence on excitation frequency, geometrical settings and mechanical properties (Berger *et al.*, 1977; Novak *et al.*, 1978; O'Rourke & Dobry, 1982; Gazetas & Dobry, 1984a,b; Shadlou & Bhattacharya, 2014). As mentioned above, the FE model is not fully representative of the real site configuration, where the rigid bedrock is significantly deeper than in the model. The shallower bedrock set for faster FE computations implies cut-off frequencies higher than expected at the real site, and therefore later onset of radiation damping and some over-prediction of dynamic amplification levels.

Dynamics of the shaker-monopile-soil system

Numerical eigenfrequency analysis

As a first step into understanding the response of the whole shaker-soil-monopile system, numerical eigenvalue analysis was carried out for the FE model in Figure 10. Due to the many degrees of freedom in the discretised system, the analysis returned multiple closely-spaced eigenfrequencies, including the first eigenvalue at 1.59 Hz associated with 'soil-only resonance'. Among the numerous numerical modes found in proximity of relevant frequencies (e.g., near the resonance frequency observed in field test results – ≈ 5.5 Hz), it was not straightforward to identify real physical modes. A heuristic mode-sorting procedure was set up by selecting eigenvectors showing significant lateral displacement of the monopile at the shaker location. Accordingly, three modes near the resonance peak were isolated at 5.67, 5.71 and 5.87 Hz – see graphical representation in Figure 12. In elastodynamics, each i^{th} mode contributes to the global response depending on the distance between external loading frequency Ω and related eigenfrequency ω_i, with a participation factor Γ_i that takes the following form for undamped multi-dof systems:

$$\Gamma_i = \frac{1}{\omega_i^2 - \Omega^2} \tag{5}$$

The above expression clarifies how the effect of the i^{th} mode on the global response vanishes for ω_i far from Ω.

Drained dynamic response

As for 'soil-only' simulations, the dynamic performance of the whole system was first analysed under fully drained conditions. Also in this case, pore pressure effects were prevented by setting high soil permeability ($k = 10^6$ m/s). There was no attempt to re-tune the soil properties in Figure 9 to improve the numerical simulation of field measurements.

Time domain analyses were performed for different loading frequencies within the selected range (0-7.5 Hz), then steady-state displacement amplitudes at the shaker and load-displacement phase differences were extracted. Drained FE results are compared to experimental data in Figure 13, and seem to capture well the overall frequency-dependence of the monopile stiffness. The minimum stiffness near 5.5 Hz is clearly reproduced, while simulations for frequencies lower than 2 Hz returned a gradual increase in dynamic stiffness as nearly static conditions are approached. On average, 3D FE results seem to slightly over-predict experimental stiffness values, most probably as a consequence of simplifying modelling assumptions.

Some sharp 'outliers' appear in the numerical results in the form of local stiffness drops at 2.5, 3.5 and even 5.5. Hz. Such outliers, not visible in experimental data, may be directly related to soil-only amplification (see Gazetas (1983)), as suggested by Figure 11a. In this respect, accurate modelling of the bottom rigid boundary would be key to improving numerical simulation results. Improved modelling of soil damping would also contribute to the same goal, in that it would smoothen the sharp outliers in Figure 13 (Gazetas, 1983). Although DISSTINCT data do not seem affected by pure soil resonance, it is worth noting that soil amplification in soft soils would likely be happening at frequencies lower than 0.5 Hz for bedrocks deeper than 100 m – i.e., within the frequency band considered in current design practice.

Further insight into FE results can be obtained by inspecting the phase difference between applied load and steady-state displacement at the shaker head. Figure 15 reveals significant increase in phase difference in the vicinity of 5.5. Hz. This observation suggests an analogy with the response of the equivalent 1dof oscillator depicted in Figure 6b, exhibiting a 90° phase shift at resonance. The agreement between FE and 1dof phase difference trends in Figure 15 clarifies the physical nature of the remarkable stiffness reduction at 5.5 Hz, which can be now attributed to global resonance in the shaker-monopile-soil system. Besides, the smoothness of experimental stiffness curves suggests that

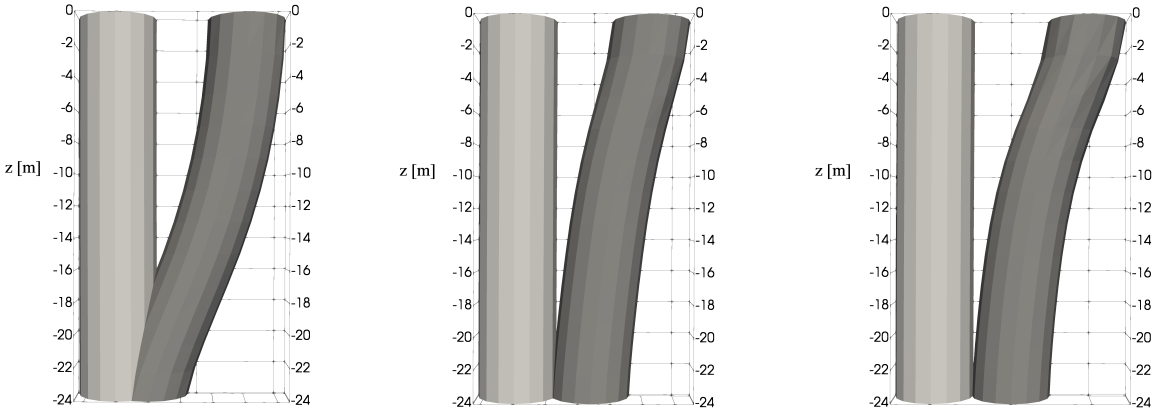

(a) 5.67 Hz **(b) 5.71 Hz** **(c) 5.87 Hz**

Fig. 12. Monopile (embedded) modal shapes for eigenvectors of the shaker-pile-soil system associated with eigenfrequencies close to experimental resonance (≈ 5.5 Hz).

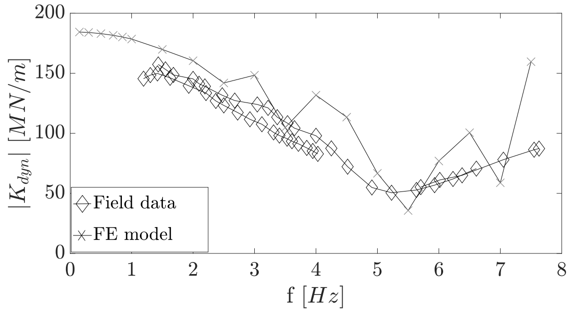

Fig. 13. Frequency dependence of monopile dynamic stiffness $|K_{dyn}|$ as emerging from field tests and FE modelling.

more energy dissipation occurred in the field tests than was reproduced by the FE model.

Also obtained from FE results is the steady-state deformed shape of the monopile at 5.5 Hz, resembling in Figure 14 the typical shape of a cantilever loaded at the free end. This outcome is in full agreement with the strain measurements in Figure 7. As none of the modes in Figure 12 represents accurately the dynamic deformed shape, the influence of several participating modes is deduced.

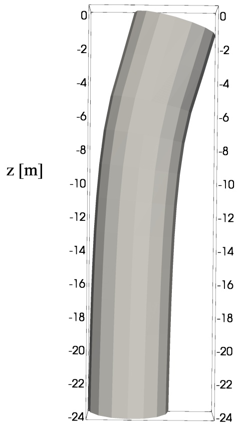

Fig. 14. Steady-state deformed shape of the monopile arising from 5.5 Hz FE calculations.

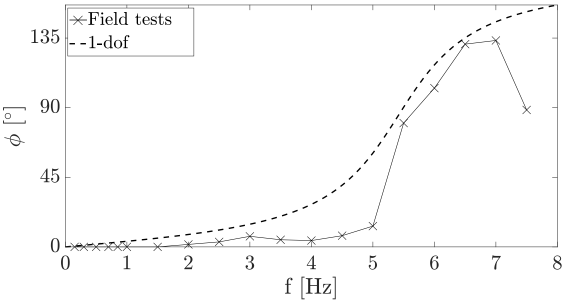

Fig. 15. Phase difference (ϕ) between applied load and steady-state shaker displacement from FE and equivalent 1dof results.

Undrained dynamic response

The FE results presented so far were obtained for fully drained conditions, i.e., by disregarding hydro-mechanical coupling effects in the soil. To assess the impact of such assumptions, the response of the system in the opposite undrained limit was numerically explored by assigning a vanishing permeability ($k = 10^{-18}$ m/s) to the whole soil domain. Accordingly, it was possible to simulate pore pressure variations caused by hindered water drainage.

As in the drained case, 'soil-only' simulations were first performed to clarify how the undrained dynamics of the soil deposit can impact the response to lateral harmonic loading of the shaker-monopile-soil system. The same approach described above for drained conditions was followed, i.e., horizontal and vertical monoharmonic point loads were applied until steady-state over a frequency range from 0 to 8 Hz. Undrained trends of amplification factor and phase difference for both loading directions are reported in Figures 16a–16b.

The undrained monopile-soil model was validated by comparing in Figure 17 the steady-state amplitudes of pore pressure variations simulated for different loading frequencies to the measurements from sensors 10-11 (Figure

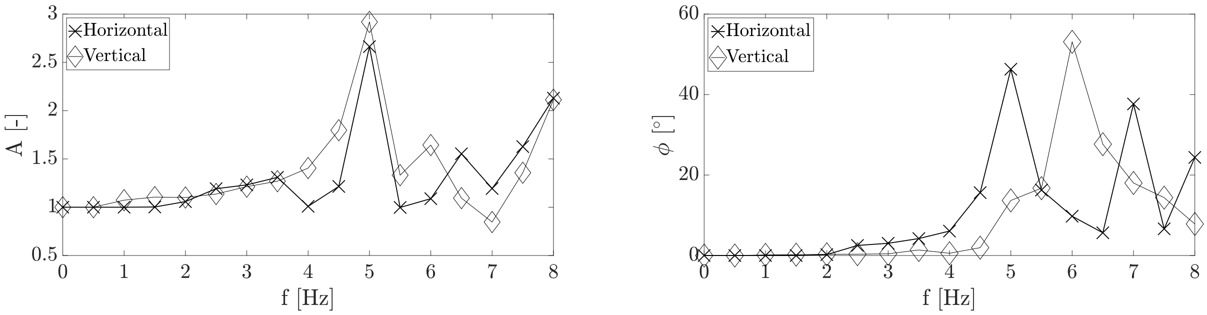

(a) Amplification factor (A) **(b) Phase difference (ϕ)**

Fig. 16. Simulated undrained steady-state responses of the soil deposit to horizontal and vertical point loading at varying loading frequency (f).

3) associated with the middle weight load case. As for the drained simulations, distinct mono-harmonic analyses were performed numerically until the attainment of steady-state; then, steady amplitudes of pore pressure variation were extracted (Figure 17c) for comparison to measured data – it was assumed that also pore pressure variations reached a steady state in each frequency step during field tests. Numerical steady-state amplitudes (e.g., from Figure 17c) were finally inserted in Figures 17a–17b over time intervals corresponding with relevant frequency steps. Computed and measured pore pressure variations share similar trends and reasonably similar values, confirming the suitability of the 3D FE model in its undrained version.

Figure 17 suggests that pore pressure effects can be very weak under low operational loads, and yet the common assumption of fully drained response in sand is not necessarily valid. The poro-elastic FE model enabled evaluation of the impact of hydro-mechanical coupling on the undrained dynamic stiffness of the monopile during small amplitude vibrations. Undrained model predictions are presented in Figure 18 together with previous drained results and experimental data. Generally, undrained conditions do not seem to significantly affect the dynamic stiffness trend, especially until the 5.5 Hz resonance. Particularly, sharp 'outliers' characterise also the undrained response trend, for instance at 4 and 7 Hz, in a way that can be again attributed to the undrained 'soil-only' amplifications visible in Figure 16a. Larger discrepancies among experimental, drained and undrained results arise in the post-resonance branch: such evidence hints that partial water drainage and relative soil-water accelerations may play a role in the monopile-soil interaction at sufficiently high frequencies. The investigation of such effects will require further refinement/generalisation of the u-p-based FE model adopted in this study.

Influence of monopile diameter

Monopile diameter is normally tuned by designers to achieve desired dynamic performance in terms of OWT first natural frequency. Additional FE calculations were performed for a larger monopile of 6 m diameter, so as to shift the natural frequency of the global system beyond the 'soil-only' resonances previously discussed.

Frequency-dependent values of amplification factor, phase difference, and dynamic lateral stiffness are plotted in Figure 19 for both diameters, 5 and 6 m. It is further confirmed that the amplification frequencies identified at 2.5 and 3.5 Hz are indeed of the 'soil-only' type (Figure 11a), therefore not affected by mononopile diameter. Additionally, the highest amplification peak for the 6 m diameter monopile occurs at a frequency lower than 5 Hz, and should be compared to the 5.5 Hz resonance hit by the 5 m monopile. This seemingly counter-intuitive outcome (a stiffer monopile may be expected to resonate at a higher frequency) can be explained via the phase difference curves in Figure 19b. Dynamic resonance is normally accompanied by input-output phase difference of 90° degrees, a circumstance that occurs at ≈ 5.6 Hz for the 5 m monopile, and near 6.8 Hz in the 6 m case – with an amplification peak lower than in the 5 m case. In light of this observation, it is recognised that the 6 m pile undergoes structural resonance near 6.8 Hz, though with an amplification lower than at 5 Hz. Such difference can only be caused by 'soil-only' amplification effects at 5 Hz, whose quantitative influence highlights the importance of accurate domain modelling in dynamic soil-structure interaction problems.

CONCLUDING REMARKS

The results of full-scale, dynamic field tests on a stiff monopile were examined to investigate the frequency-dependence of soil-pile interaction at a sandy site. To support the interpretation of field data, 3D FE modelling was undertaken, with soil parameters derived from pre-installation site data.

For the weak vibrations induced by the pile-shaking device, the good agreement between experimental and numerical results supported the soundness of most simplifying assumptions, such as the idealisation of linear elastic soil skeleton. Low variations in pore pressures (with respect to hydrostatic values) were predicted when modelling fully undrained conditions – another outcome compatible with field measurements. The latter observation confirmed the suitability of neglecting pore pressure effects for weakly loaded monopiles in sand; however, claiming that water drainage (and volume changes) are fully allowed in the soil around the pile may prove inaccurate in some cases. Obviously, the discussion about pore pressure effects will assume more relevance for higher load levels, under which soil non-linearity and cyclic effects are more pronounced (Kementzetzidis *et al.*, 2019; Liu *et al.*, 2019).

The dynamic response of the monopile exhibited remarkable frequency-dependency at loading rates higher than currently considered in design. Significant energy dissipation was also observed, with a global viscous damping ratio of about 16% deduced from field data. Wave radiation

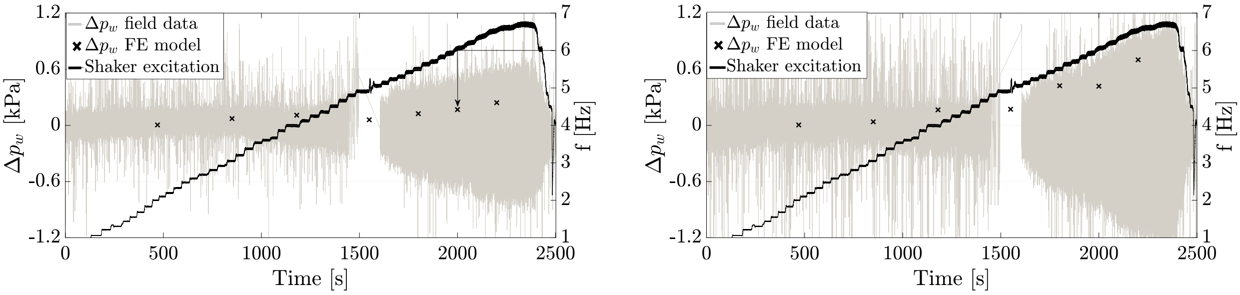

(a) measured pore pressure variations – sensor 10.

(b) measured pore pressure variations – sensor 11.

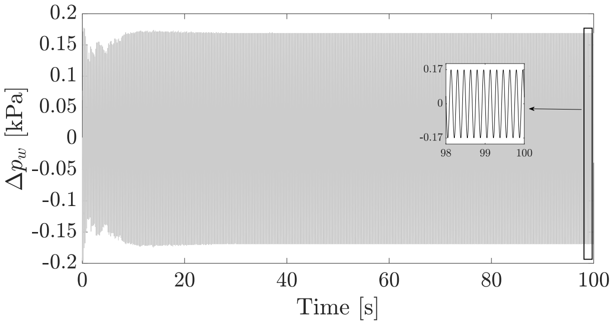

(c) simulation of pore pressure variation under 6 Hz harmonic loading at the location of sensor 10.

Fig. 17. Comparison between measured and simulated pore pressure variations (middle weight load case). The arrow in (a) points to a specific steady-state amplitude ($\Delta p_w = 0.17$ kPa), resulting from the numerical results illustrated in (c).

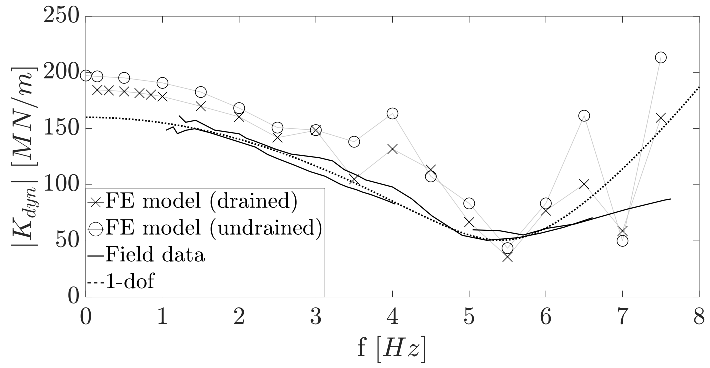

Fig. 18. Influence of drainage conditions on the monopile dynamic stiffness.

in the soil is believed to largely, but not exclusively, contribute to such dissipation.

Inspection of FE results under varying frequency, pile diameter and drainage conditions led to recognition of the wide range of soil-monopile interaction scenarios caused by dynamic effects. As larger turbines are installed in more dynamically-active environments (deeper waters and/or seismic regions), considerations regarding wave motion in the surrounding soil will become increasingly relevant to geotechnical design.

ACKNOWLEDGEMENTS

The authors express their gratitude to the DISSTINCT consortium (project number TKIW02001) for allowing full access to field data.

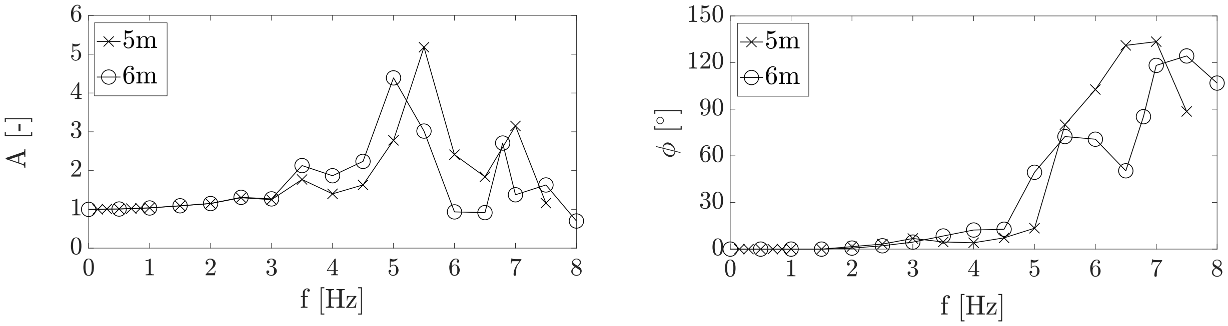

(a) Amplification factor (A)

(b) Phase difference (ϕ)

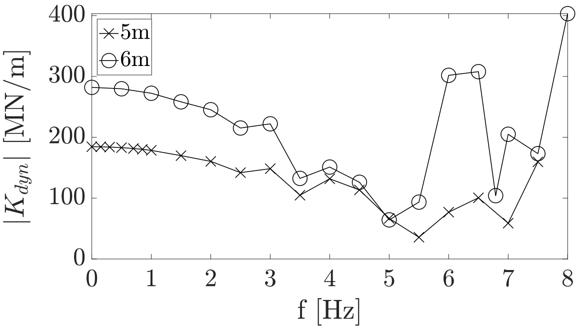

(c) Dynamic stiffness ($|K_{dyn}|$)

Fig. 19. Simulated steady-state responses of laterally loaded monopiles of 5 m and 6 m diameter.

LIST OF SYMBOLS

Greek symbols

β, γ	Newmark's time integration parameters
Γ_i	modal participation factor associated with i$^{\text{th}}$ mode
Δp_w	pore water pressure variation
ε	axial strain
ζ^{1dof}	damping ratio of the equivalent 1dof system
ζ_{steel}	steel damping ratio
ν	soil Poisson's ratio
ρ	saturated mass density for sand
ρ_f	mass density of pore fluid
ρ_s	mass density of soil grains
σ, σ'	soil stress tensor (total and effective)
ϕ	phase difference/angle
Ω	angular excitation/loading frequency
ω_i	eigenfrequency associated with i$^{\text{th}}$ mode

Latin symbols

A	amplification factor
C^{1dof}	viscous damping coefficient for the equivalent 1dof system
D	Soil stiffness tensor (D_{ijkl})
D_R	soil relative density
E	Young's modulus of elasticity
$\bar{E}$	1D (oedometer) stiffness modulus
F	applied load amplitude
f_s	CPT sleeve friction
f_n	n^{th} natural frequency of the soil deposit
f_{res}	resonance frequency
G	transfer function
g	Earth's gravity acceleration
H_w	water depth
K_{dyn}	lateral dynamic stiffness of the monopile
$\lvert K_{dyn}^{1dof} \rvert$	absolute value of the dynamic stiffness of the equivalent 1dof system
K_0^{1dof}	static stiffness of the equivalent 1dof system
K_f	fluid bulk modulus
K_s	soil grains bulk modulus
k, k'	soil permeability coefficients in the static and dynamic versions of Darcy law
L	monopile length
L_{emb}	embedded monopile length
M^{1dof}	mass of the equivalent 1dof system
M_{sh}	lumped shaker mass
m_e	rotating mass
n	soil porosity
p_w	pore water pressure
q_c	CPT cone resistance
R	lever arm
t	time
U	shaker displacement
u	soil displacement
$\bar{U}$	shaker steady-state displacement amplitude
$\bar{u}$	soil steady-state displacement amplitude
u_{inp}	bedrock steady-state displacement amplitude
u_{static}	static soil displacement
V_s	shear wave velocity
z	depth

REFERENCES

Angelides, D. C. & Roesset, J. M. (1981). Nonlinear lateral dynamic stiffness of piles. *Journal of Geotechnical and Geoenvironmental Engineering* **107**, No. ASCE 16635 Proceeding.

Anusic, I., Eiksund, G. R., Meissl, S. & Liingaard, M. A. (2017). Study of a new installation technique for large diameter monopiles. In *Proceedings of 19th International Conference on Soil Mechanics and Geotechnical Engineering (ICSMGE2017). Seoul, South Korea*, pp. 2261–2264.

Arany, L. & Bhattacharya, S. (2018). Simplified load estimation and sizing of suction anchors for spar buoy type floating offshore wind turbines. *Ocean Engineering* **159**, 348–357.

Archer, C., Simão, H., Kempton, W., Powell, W. & Dvorak, M. (2017). The challenge of integrating offshore wind power in the us electric grid. part i: Wind forecast error. *Renewable energy* **103**, 346–360.

Berger, E., Mahi, S. A., Pyke, R. *et al.* (1977). Simplified method for evaluating soil-pile-structure interaction effects. In *Offshore Technology Conference*, Offshore Technology Conference.

Bienen, B., Klinkvort, R. T., O'Loughlin, C., Zhu, F. & Byrne, B. (2018). Suction caissons in dense sand, part ii: vertical cyclic loading into tension. *Géotechnique* , 1–15.

Biot, M. (1956). Theory of elastic waves in a fluid-saturated porous solid. 1. low frequency range. *J. Acoust. Soc. Am.* **28**, 168–178.

BS EN (1991). 1-4: 2005 eurocode 1: Actions on structures - general actions - wind actions.

Byrne, B. W., Burd, H. J., Zdravkovic, L., Abadie, C. N., Houlsby, G. T., Jardine, R. J., Martin, C. M., McAdam, R. A., Pacheco Andrade, M., Pedro, A. M. *et al.* (2019). Pisa design methods for offshore wind turbine monopiles. In *Offshore Technology Conference*, Offshore Technology Conference.

Chan, A. H.-C. (1988). *A unified finite element solution to static and dynamic problems of geomechanics*. Ph.D. thesis, Swansea University.

Chancham, C., Waewsak, J. & Gagnon, Y. (2017). Offshore wind resource assessment and wind power plant optimization in the gulf of thailand. *Energy* **139**, 706–731.

Corciulo, S., Zanoli, O. & Pisanò, F. (2017). Transient response of offshore wind turbines on monopiles in sand: role of cyclic hydro–mechanical soil behaviour. *Computers and Geotechnics* **83**, 221–238.

Dobry, R. & Gazetas, G. (1988). Simple method for dynamic stiffness and damping of floating pile groups. *Geotechnique* **38**, No. 4, 557–574.

Doherty, P. & Gavin, K. (2012). Laterally loaded monopile design for offshore wind farms. *Proceedings of the Institution of Civil Engineers - Energy* **165**, No. 1, 7–17.

Dutch Ministry of Economic Affairs (2016). Energy report: transition to sustainable energy. *Technical report*, Ministry of Economic Affairs, The Netherlands, URL `https://www.government.nl/documents/reports/2016/04/28/energy-report-transition-tot-sustainable-energy`.

Elgamal, A., Yang, Z. & Parra, E. (2002). Computational modeling of cyclic mobility and post-liquefaction site response. *Soil Dynamics and Earthquake Engineering* **22**, No. 4, 259–271.

Fan, S., Bienen, B. & Randolph, M. F. (2019). Centrifuge study on effect of installation method on lateral response of monopiles in sand. *International Journal of Physical Modelling in Geotechnics* , 1–35.

Galavi, V., Beuth, L., Coelho, B. Z., Tehrani, F. S., Hölscher, P. & Van Tol, F. (2017). Numerical simulation of pile installation in saturated sand using material point method. *Procedia Engineering* **175**, 72–79.

Gazetas, G. (1983). Analysis of machine foundation vibrations: state of the art. *International Journal of Soil Dynamics and Earthquake Engineering* **2**, No. 1, 2–42.

Gazetas, G. & Dobry, R. (1984a). Horizontal response of piles in layered soils. *Journal of Geotechnical engineering* **110**, No. 1, 20–40.

Gazetas, G. & Dobry, R. (1984b). Simple radiation damping model for piles and footings. *Journal of Engineering Mechanics* **110**, No. 6, 937–956.

Graff, K. F. (2012). *Wave motion in elastic solids.* Courier Corporation.

Han, B., Zdravkovic, L. & Kontoe, S. (2016). Numerical and analytical investigation of compressional wave propagation in saturated soils. *Computers and Geotechnics* **75**, 93–102.

He, R., Kaynia, A. M. & Zhang, J. (2019). A poroelastic solution for dynamics of laterally loaded offshore monopiles. *Ocean Engineering* **179**, 337–350.

Houlsby, G., Kelly, R., Huxtable, J. & Byrne, B. (2005). Field trials of suction caissons in clay for offshore wind turbine foundations. *Géotechnique* **55**, No. 4, 287–296.

Houlsby, G., Kelly, R., Huxtable, J. & Byrne, B. (2006). Field trials of suction caissons in sand for offshore wind turbine foundations. *Géotechnique* **56**, No. 1, 3–10.

Hughes, T. J. R. (1987). *The finite element method: linear static and dynamic finite element analysis.* Prentice-Hall.

Kagawa, T. & Kraft, L. M. (1980). Lateral load-deflection relationships of piles subjected to dynamic loadings. *Soils and Foundations* **20**, No. 4, 19–36.

Kallehave, D., Byrne, B. W., LeBlanc Thilsted, C. & Mikkelsen, K. K. (2015). Optimization of monopiles for offshore wind turbines. *Philosophical Transactions of the Royal Society A: Mathematical, Physical and Engineering Sciences* **373**, No. 2035, 20140100.

Kallehave, D., Thilsted, C. L. & Liingaard, M. (2012). Modification of the API p-y formulation of initial stiffness of sand. In *Proceedings of Offshore Site Investigation and Geotechnics: Integrated Technologies - Present and Future. London, UK*, Society of Underwater Technology, pp. 465–472.

Kementzetzidis, E., Corciulo, S., Versteijlen, W. G. & Pisanò, F. (2019). Geotechnical aspects of offshore wind turbine dynamics from 3D non-linear soil-structure simulations. *Soil Dynamics and Earthquake Engineering* **120**, 181–199.

Kementzetzidis, E., Versteijlen, W. G., Nernheim, A. & Pisanò, F. (2018). 3D FE dynamic modelling of offshore wind turbines in sand: Natural frequency evolution in the pre-to after-storm transition. In *Numerical Methods in Geotechnical Engineering IX, Volume 2*, CRC Press, pp. 1477–1484.

Kontoe, S., Zdravkovic, L. & Potts, D. M. (2008). An assessment of time integration schemes for dynamic geotechnical problems. *Computers and geotechnics* **35**, No. 2, 253–264.

Kuhlemeyer, R. L. (1979). Static and dynamic laterally loaded floating piles. *Journal of Geotechnical and Geoenvironmental Engineering* **105**, No. ASCE 14394.

Liu, H. Y., Abell, J. A., Diambra, A. & Pisanò, F. (2019). Modelling the cyclic ratcheting of sands through memory-enhanced bounding surface plasticity. *Géotechnique* **69**, No. 9, 783–800.

Lysmer, J. & Kuhlemeyer, R. L. (1969). Finite dynamic model for infinite media. *Journal of the Engineering Mechanics Division* **95**, No. 4, 859–878.

Mattar, C. & Borvarán, D. (2016). Offshore wind power simulation by using wrf in the central coast of chile. *Renewable Energy* **94**, 22–31.

McGann, C. R., Arduino, P. & Mackenzie-Helnwein, P. (2015). A stabilized single-point finite element formulation for three-dimensional dynamic analysis of saturated soils. *Computers and Geotechnics* **66**, 126–141.

McKenna, F. T. (1997). *Object-oriented finite element programming: frameworks for analysis, algorithms and parallel computing.* Ph.D. thesis, University of California, Berkeley.

Mylonakis, G. & Gazetas, G. (1999). Lateral vibration and internal forces of grouped piles in layered soil. *Journal of Geotechnical and Geoenvironmental Engineering* **125**, No. 1, 16–25.

Newman, J. N. (1977). *Marine hydrodynamics.* MIT press.

Novak, M. (1974). Dynamic stiffness and damping of piles. *Canadian Geotechnical Journal* **11**, No. 4, 574–598.

Novak, M., Aboul-Ella, F. & Nogami, T. (1978). Dynamic soil reactions for plane strain case. *Journal of the Engineering Mechanics Division* **104**, No. 4, 953–959.

O'Rourke, M. J. & Dobry, R. (1982). Spring and dashpot coefficients for machine foundations on piles. *Special Publication* **78**, 177–198.

Paulsen, B. T., de Sonneville, B., van der Meulen, M. & Jacobsen, N. G. (2019). Probability of wave slamming and the magnitude of slamming loads on offshore wind turbine foundations. *Coastal Engineering* **143**, 76–95.

Pisanò, F. (2019). Input of advanced geotechnical modelling to the design of offshore wind turbine foundations. In *Proceedings of 17th European Conference on Soil Mechanics and Geotechnical Engineering (ECSMGE2019). Reykjavík, Iceland*, International Society of Soil Mechanics and Geotechnical Engineering (ISSMGE).

Pisanò, F. & Gavin, K. G. (2017). General report for TC209 - Offshore Geotechnics. In *Proceedings of 19th International Conference on Soil Mechanics and Geotechnical Engineering (ICSMGE2017). Seoul, South Korea.*

Pisanò, F. & Pastor, M. (2011). 1D wave propagation in saturated viscous geomaterials: improvement and validation of a fractional step Taylor–Galerkin finite element algorithm. *Computer methods in applied mechanics and engineering* **200**, No. 47-48, 3341–3357.

Shadlou, M. & Bhattacharya, S. (2014). Dynamic stiffness of pile in a layered elastic continuum. *Geotechnique* **64**, No. 4, 303.

Shadlou, M. & Bhattacharya, S. (2016). Dynamic stiffness of monopiles supporting offshore wind turbine generators. *Soil Dynamics and Earthquake Engineering* **88**, 15–32.

Skau, K. S., Page, A. M., Kaynia, A. M., Løvholt, F., Norén-Cosgriff, K., Sturm, H., Andersen, H., Nygard, T., Jostad, H. P., Eiksund, G. *et al.* (2018). REDWIN–REDucing cost in offshore WINd by integrated structural and geotechnical design. In *Journal of Physics: Conference Series*, vol. 1104, IOP Publishing, p. 012029.

Tehrani, F. S., Nguyen, P., Brinkgreve, R. B. & van Tol, A. F. (2016). Comparison of press-replace method and material point method for analysis of jacked piles. *Computers and Geotechnics* **78**, 38–53.

Tsai, Y.-C., Huang, Y.-F. & Yang, J.-T. (2016). Strategies for the development of offshore wind technology for far-east countries–a point of view from patent analysis. *Renewable and Sustainable Energy Reviews* **60**, 182–194.

Versteijlen, W. (2018). *Identification of effective 1D soil models for large-diameter offshore wind turbine foundations based on in-situ seismic measurements and 3D modelling.* Ph.D. thesis, Delft University of Technology.

Versteijlen, W., Renting, F., van der Valk, P., Bongers, J., van Dalen, K. & Metrikine, A. (2017a). Effective soil-stiffness validation: shaker excitation of an in-situ monopile foundation. *Soil Dynamics and Earthquake Engineering* **102**, 241 – 262, doi:https://doi.org/10.1016/j.soildyn.2017.08.003, URL `http://www.sciencedirect.com/science/article/pii/S0267726117301008`.

Versteijlen, W., Renting, F., van der Valk, P., Bongers, J., van Dalen, K. & Metrikine, A. (2017b). Effective soil-stiffness validation: Shaker excitation of an in-situ monopile foundation. *Soil Dynamics and Earthquake Engineering* **102**, 241–262.

Wang, X., Zeng, X., Li, J., Yang, X. & Wang, H. (2018). A review on recent advancements of substructures for offshore wind turbines. *Energy conversion and management* **158**, 103–119.

Watanabe, K., Pisanò, F. & Jeremić, B. (2017). Discretization effects in the finite element simulation of seismic waves in elastic and elastic-plastic media. *Engineering with Computers* **33**, No. 3, 519–545.

Zienkiewicz, O. C., Chan, A. H. C., Pastor, M., Schrefler, B. A. & Shiomi, T. (1999). *Computational geomechanics.* Wiley Chichester.

Zienkiewicz, O. C., Chang, C. T. & Bettess, P. (1980). Drained, undrained, consolidating and dynamic behaviour assumptions in soils. *Géotechnique* **30**, No. 4, 385–395.

APPENDIX

The dynamic response of a layered soil deposit has been studied throughout this work using a two-phase 3D FE model based on the well-known *u-p* formulation (Zienkiewicz *et al.*, 1999). Compared to its original conception (Zienkiewicz *et al.*, 1980), a simpler *u-p* formulation ('consolidation form') is adopted in the OpenSees FE software (Elgamal *et al.*, 2002), so that fluid inertial terms (not only soil-fluid relative accelerations) are completely neglected (Chan, 1988). Using the same two-phase FE model, both drained and undrained conditions have been analysed by setting, respectively, very high or very low values of soil permeability. Obviously, a simpler one-phase model could be adopted for uncoupled drained analyses, as long as the saturated soil-fluid mass density is set to represent an underwater soil deposit.

3D one-phase and two-phase dynamic equations are compared in Table A1 (Equations (A1)-(A4)), where ρ indicates the mass density of fluid-saturated soil, and $1/Q = n/K_f + (1-n)/K_s$ the overall compressibility of solid and fluid constituents (average of the corresponding bulk moduli, K_f and K_s, weighted on the porosity n) – all symbols are defined in the notation list. It is readily apparent that, if elastic, stress-independent behaviour is considered for the soil skeleton, then the *u-p*/consolidation model reduces exactly to the one-phase/drained model as the soil permeability k' tends to infinity. It should be noted that, in the dynamic version of the Darcy law, the hydraulic conductivity k' ([length]^3[time]/[mass]) is introduced in the relationship between (relative) discharge velocity and pore pressure gradient (instead of the hydraulic head gradient). The more usual permeability coefficient k ([length/time]) can be obtained as $k = k'\rho_f g$, where ρ_f and g stand for fluid density and gravity acceleration, respectively (Zienkiewicz *et al.*, 1999).

The same conclusion is further corroborated in Table A1 (Equations (A5)-(A7)) for the case of a 1D elastic soil column under forced harmonic motion. The steady-state eigenvalue problems associated with (A5), both one-phase and two-phase/incompressible, are formulated in (A6) and solved for the following boundary conditions: (i) free surface at the top, (ii) rigid/impervious bedrock at $y = H$, (iii) imposed harmonic motion at the bedrock, $u(H,t) = u_{inp}(\Omega)\exp(i\Omega t)$, with the amplitude u_{inp} possibly a function of the input circular frequency Ω. The two-phase eigenfunction $\bar{u}$ tends to its one-phase counterpart as $k' \to \infty$ (further details about the 1D two-phase solution available in Pisanò & Pastor (2011)), which re-confirms the legitimacy of using a *u-p*/consolidation model to recover fully drained conditions as a special case.

Governing Equations	one-phase	two-phase	
mixture momentum balance	$\rho\ddot{u}_i = \sigma_{ij,j}$	$\rho\ddot{u}_i = \sigma_{ij,j} = \sigma'_{ij,j} - p_{w,i}$	(A1)
elastic stress-strain law	$\sigma_{ij} = \frac{1}{2}D_{ijkl}\left(u_{k,l} + u_{l,k}\right)$	$\sigma'_{ij} = \frac{1}{2}D_{ijkl}\left(u_{k,l} + u_{l,k}\right)$	(A2)
balance of fluid momentum and mass + Darcy law	—	$k' p_{w,ii} = \dot{u}_{i,i} + \frac{\dot{p}_w}{Q}$	(A3)
Combined form (A1)+(A2)+(A3)	$\rho\ddot{u}_{i,i} = \frac{1}{2}\left[D_{ijkl}\left(u_{k,l} + u_{l,k}\right)\right]_{,ji}$	$\rho\ddot{u}_{i,i} = \frac{1}{2}\left[D_{ijkl}\left(u_{k,l} + u_{l,k}\right)\right]_{,ji} - \frac{\dot{u}_{i,i} + \dot{p}_w/Q}{k'}$	(A4)
1D elastic soil column under harmonic excitation			
1D governing equation	$\ddot{u} - \frac{\bar{E}}{\rho}u_{,yy} = 0$	$\left[\ddot{u} - \frac{\bar{E}}{\rho}u_{,yy} + \frac{1}{k'\rho}\left(1 + \frac{\bar{E}}{Q}\right)\dot{u}\right]_{,yy} - \frac{1}{Qk'}\dddot{u} = 0$	(A5)
eigenvalue problem $(Q \to \infty)$	$\bar{u}_{,yy} + \frac{\rho\Omega^2}{\bar{E}}\bar{u} = 0$	$\left[\bar{u}_{,yy} + \left(\frac{\rho\Omega^2}{\bar{E}} - \frac{\Omega}{k'\bar{E}}i\right)\bar{u}\right]_{,yy} = 0$	(A6)
eigenfunction $\bar{u}$(y,Ω) $(Q \to \infty)$	$\frac{\cos\left(\sqrt{\frac{\Omega^2\rho}{\bar{E}}}y\right)}{\cos\left(\sqrt{\frac{\Omega^2\rho}{\bar{E}}}H\right)}u_{inp}(\Omega)$	$\frac{\cos\left(\sqrt{\frac{\Omega^2\rho}{\bar{E}} - \frac{\Omega}{k'\bar{E}}i}\;y\right)}{\cos\left(\sqrt{\frac{\Omega^2\rho}{\bar{E}} - \frac{\Omega}{k'\bar{E}}i}\;H\right)}u_{inp}(\Omega)$	(A7)

Table A1. Dynamic soil modelling: 1-phase vs 2-phase ($\boldsymbol{u}$-$\boldsymbol{p}$/consolidation) formulations. Notation/conventions: (i) index notation for space derivatives, dots used for time differentiation; (ii) total and effective stresses denoted by σ_{ij} and σ'_{ij}, respectively; (iii) opposite sign conventions adopted for solid stresses (positive if tensile) and pore pressure (positive if compressive); (iv) the incompressible limit $(Q \to \infty)$ is considered in (A6)-(A7) with no loss of generality.